



## Research Article

# Optimization of Switching Control and Microgrid Energy Management System with Alternate Arm Converter Based on Bacterial Foraging Algorithm

S. T. Rama <sup>1,2</sup> and V. Rajini <sup>3</sup>

<sup>1</sup>Research Scholar, Department of EEE, Sathyabama Institute of Science and Technology, Jeppiaar Nagar, Chennai, Tamilnadu, India

<sup>2</sup>Department of EEE, Dr.M.G.R Educational and Research Institute, Maduravoyal, Chennai, Tamilnadu, India

<sup>3</sup>Department of EEE, SSN College of Engineering, Kalavakkam, Chennai, Tamilnadu, India

Correspondence should be addressed to S. T. Rama; rama.eee@drmgrdu.ac.in

Received 21 April 2023; Revised 23 August 2023; Accepted 27 September 2023; Published 18 October 2023

Academic Editor: K. Jyotheeswara Reddy

Copyright © 2023 S. T. Rama and V. Rajini. This is an open access article distributed under the Creative Commons Attribution License, which permits unrestricted use, distribution, and reproduction in any medium, provided the original work is properly cited.

The global demand of electrical power has increased enormously due to various reasons such as fast-changing and challenging technologies, climatic change, economic growth, and lifestyle of mankind. Due to global warming issues and the depletion of conventional sources of power generation, the utilization of renewable energy sources has drastically increased. So, many challenges exist in integrating the microgrid with AC grid and load. The alternative arm converter (AAC) is among the most innovative converter topologies used in high voltage direct current (HVDC) applications. This research work presents a new control strategy to generate pulses to trigger the switches in the AAC in a proper sequence to obtain a smooth output waveform. The AAC output is controlled by implementing various controllers such as the proportional-integral-derivative (PID) controller, fractional order PID (FOPID) controller, and FOPID controller tuned by metaheuristic algorithm-bacterial foraging optimization technique (BFOT). Also, a comparative analysis is performed based on the spectral analysis of the output voltage obtained. In comparison to other controllers, the FOPID controller optimized by the bacterial foraging optimization technique (BFOT) produced the least total harmonic distortion (THD) of the AAC output voltage. In addition, this paper also discusses about the performance and analysis on the design of an energy management system (EMS) to optimally utilize the energy sources such as PV system, wind system, and battery based on their availability which feed the AAC. The energy management system controls the entire integrated system in association with an integrated CUK-SEPIC converter to fulfil the load demand at the point of common coupling, either from the microgrid or the AC grid. A nine-level AAC model is designed integrating the microgrid, grid, and industrial loads with an energy management system using MATLAB/Simulink. The performance parameters of the entire model are analysed at every stage to provide stabilized output to meet the load demand.

## 1. Introduction

Concerns over the energy issue and the environmental harm caused by fossil fuels have grown in recent years, and this has led to the broad application of renewable energy sources (RESs) including solar, biomass, wind, and geothermal energy. However, wind and solar energy are inherently volatile and intermittent, and adding these RESs directly to power networks may cause issues with reliability, energy

efficiency, and power quality [1]. Because of their high volatility and randomness, dispersed renewable energy sources provide substantial difficulties to the microgrid's ability to operate economically and reliably [2]. Accurate generation schedule preparation is exceedingly difficult because to the numerous stochastic resources and the load requirement [3]. However, to ensure a consistent supply of electricity and efficient use of the battery storage, a microgrid must be equipped with an energy management system

(EMS) to efficiently dispatch and distribute various energy supplies based on their availability and associated costs [4]. The main intention of designing an efficient energy management system (EMS) is to accomplish many objectives, including lowering power losses, managing energy fluctuations, maximizing the use of alternative energy sources, and increasing the system load factor, among others [5].

The novelty of this research is presenting the design of an optimized control strategy for obtaining the desired output across alternate arm converter (AAC) and designing an efficient embedded energy management system in integrating a microgrid with alternate arm converter (AAC) and AC grid to meet the load demand. Instead of focusing solely on AC grid supply, this strategy focuses on the maximum optimized usage of available solar PV energy, wind energy, and energy stored in the battery. In this configuration, an integrated CUK-SEPIC dualinput converter decides the input to AAC based on the control provided by the energy management system.

The following list summarises on the main contributions of the research work:

- (a) A nine-level alternate arm converter model
- (b) A comparative analysis on the spectral analysis of the output voltage of AAC obtained by incorporating different controllers which is supported by the design in MATLAB/Simulink and Fast Fourier transform analysis waveforms
- (c) An optimized control strategy based on bacterial foraging optimization algorithm is incorporated in AAC to obtain a desired and smooth output which is supported by its results
- (d) An efficient energy management system is designed to monitor and optimally utilize the energy resources available to meet the load

The rest of the paper is organized as follows: The operation and control strategies implemented in AAC are discussed in the preliminaries. The proposed methodology of the work is presented in Section 3, and in Sections 4 and 5, the design and operation of EMS, results, and discussion are presented.

## 2. Preliminaries

**2.1. Alternate Arm Converter.** The alternate arm converter (AAC) is one of the latest topologies among voltage source converter (VSC) family which can be implemented in telecommunication industry, railway traction and many other applications. The notable features of alternate arm converter (AAC) superior to modular multilevel converter (MMC) are DC fault tolerant capability, capability to pull through AC faults and reduced number of submodules by half in each leg when compared with MMC for the same power rating, etc, [6]. The AAC topology is framed by stack of full bridge submodules (SM) connected in a cascaded manner. These cascaded submodules are called as wave-shaping circuits which are attached to a two-level converter, namely, director switch (DS) in series with an inductor

(Larm) and an equivalent series resistance (ESR-Rarm) forming an arm. There are two arms in each phase/leg, the upper arm and lower arm. A symmetrical design is adopted in both the arms. This leg design is incorporated for other phases but with 120 degrees apart. The director switch (DS) is the most important component in this configuration which alternates either the upper arm or the lower arm to operate individually. The main purpose of DS is to alter the current flow between the upper arm and the lower arm from which the converter has obtained its name as "Alternate Arm Converter." The advantage of this topology is to reduce the power loss caused due to the continuous flow of current in both the arms even when only one of the arms is contributing to the output when compared to other topologies such as flying capacitor, neutral point clamped (NPC) inverter, cascaded H-bridge multilevel inverter, diode-clamped multilevel inverters, and modular multilevel converters.

A submodule comprises of either half bridge or full bridge configuration as shown in Figure 1.

In case of half bridge configuration, S1 is turned ON and S2 is turned OFF in an alternative pattern in order to prevent short-circuit condition when both the switches are switched ON simultaneously. Depending on the direction of the current iupper or ilower, capacitor connected across S1 and S2 is charged or discharged. In case of a full bridge, switches S1 and S4 are triggered ON simultaneously while S2 and S3 are in OFF state. When S2 and S3 are ON, S1 and S4 are in an OFF condition to generate an output voltage across the terminals in the positive and negative cycles.

**2.2. Operation.** The alternate arm converter can be operated as an inverter as well as a rectifier. In this research, the AAC functions as an inverter. A DC voltage of  $V_{dc}/2$  is applied across the upper arm and lower arm of AAC. The configuration of a single-phase nine-level AAC is depicted in Figure 2. Let us consider that there are P number of full bridge submodules connected in cascade, and this cascade connection is joined with an inductor Lupper arm and director switch DS1 in series to form the upper arm as shown in Figure 2. Another arm with the same symmetrical configuration forms the lower arm. An AC output voltage can be measured between the point of meeting of these two arms and the ground by connecting a load. A smooth and controlled AC output voltage is obtained by adapting a proper switching sequence to either insert or bypass a submodule into the path of current flow to be a part in generating the output voltage. The director switch (DS) consists of a few IGBTs connected in series. The switches present in the submodules and director switches are triggered by the phase shift PWM technique.

A smooth output is obtained without the need of filters which contributes in the reduction of the converter cost by increasing the number of submodules in each arm. A three-phase output voltage is obtained by connecting the symmetrical topology together displaced with 120 degrees apart as R, Y, and B phase/leg. A circulating current  $i_{circ}$  flows through the 6 arms due to the capacitor voltage imbalance in the submodules present in the upper arm and lower arms

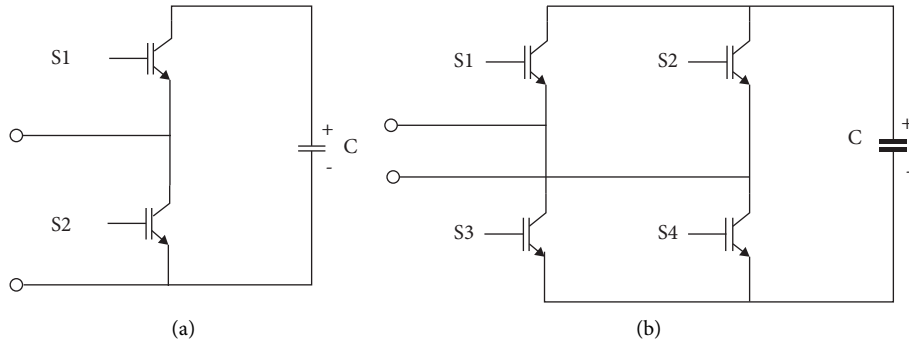


FIGURE 1: (a) Half bridge submodule; (b) full bridge submodule.

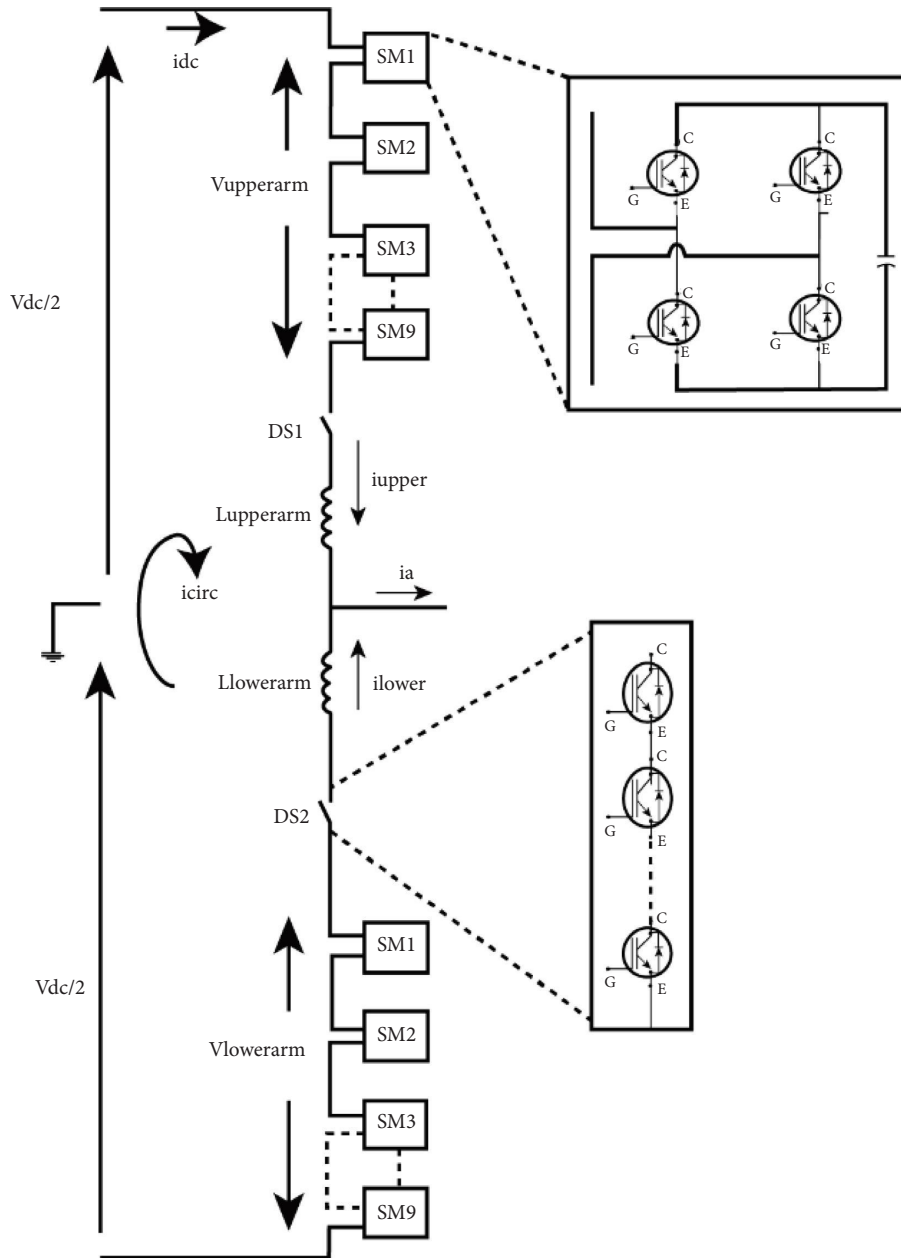


FIGURE 2: Configuration of a single-phase nine-level AAC.

which is reduced/suppressed by the arm inductors,  $L_{\text{upperarm}}$  and  $L_{\text{lowerarm}}$  in each leg. The currents  $i_{\text{dc}}$  flows from the DC link,  $i_{\text{upper}}$  and  $i_{\text{lower}}$  are the arm currents, and  $i_a$  is the current that flows through the load connected between the midpoint of the leg and ground.

**2.3. Control Strategy of AAC.** The research focuses on an efficient control strategy to control the real and reactive power in grid-tied inverters and to obtain minimum THD in the output voltage for an AAC. The integration of the microgrid and inverter with the AC grid is not an easy task to interface, as proper/right synchronization must be developed to avoid unbalance between them neglecting which may lead to unbalancing of loads, damage to the entire system, poor power quality, unstable operation of the grid and in severe cases outage may also occur which have to be taken care. In order to transfer maximum power from renewable energy sources to the grid, the frequency, and the phase angle of the output current and voltage of the inverter must be synchronized which can be implemented using different control strategies incorporating the concept of the power transfer theorem [7].

In order to synchronize the microgrid with the AC grid, an efficient control strategy must be adapted which also improves the performance of AAC by generating the proper switching pattern to switch on the IGBT switches in the SMs and DSs. There are various traditional control strategies such as current control method, voltage control method, space vector control technique, decoupled control method, and direct power control which are implemented in grid-tied and standalone inverters.

**2.3.1. Proposed Control Strategy for AAC.** The proposed control strategy for AAC integrating the grid and the alternate energy sources feeding the load is shown in Figure 3. A DC voltage of  $V_{\text{dc}} = 10 \text{ kV}$  is applied as input to the AAC which generates an AC output voltage across the load  $R_{\text{load}}$ . A smooth and regulated AC output voltage is obtained by adopting an efficient control strategy, the synchronous reference frame vector current control method with phase locked loop (SRF-PLL) is used to generate the gating pulses to trigger the IGBT switches. The synchronous reference frame control or dq control employs the transformation of 3 phase AC signals to 2 phase rotating components using Park and Clarke transformation techniques. The dq0 ( $H_d$ ,  $H_q$ , and  $H_0$ ) voltages and currents are obtained by transforming the actual/measured ( $H_a$ ,  $H_b$ , and  $H_c$ ) voltages and currents of AAC using the Clarke–Park transformation method which is depicted in equation (1). The real power can be regulated by the  $d$  axis component and the reactive power by the  $q$  axis [8–11]. The idea behind this transformation is to analyse the complex signal easily in 2 axes, the direct axis (i.e., the real axis) and the quadrature axis (i.e., the imaginary axis) such that the output of the inverter is made to rotate with the frequency of the grid voltage to synchronize the inverter voltage with the grid. The SRF-PLL is implemented to obtain the phase angle and frequency to synchronize with the grid parameters. The PLL's primary function in a three-phase system is to precisely evaluate the phase difference between the input and output voltage and current waveforms. The angle calculated by PLL is taken to be  $\Theta$  and the actual angle is taken to be  $\omega * t$  which is given by equation (2). When the PLL traces the phase angle and if it is nearly equal to the actual voltage vector angle ( $\omega t - \Theta$ ), then it can be expressed as in equation (3).

$$\begin{bmatrix} H_d \\ H_q \\ H_0 \end{bmatrix} = \frac{\sqrt{2}}{\sqrt{3}} \begin{bmatrix} \cos \omega t & -\sin \omega t & \frac{\sqrt{2}}{2} \\ \cos\left(\omega t - \frac{2\pi}{3}\right) & -\sin\left(\omega t - \frac{2\pi}{3}\right) & \frac{\sqrt{2}}{2} \\ \cos\left(\omega t + \frac{2\pi}{3}\right) & -\sin\left(\omega t + \frac{2\pi}{3}\right) & -\frac{\sqrt{2}}{2} \end{bmatrix} \begin{bmatrix} H_a \\ H_b \\ H_c \end{bmatrix}, \quad (1)$$

$$\begin{bmatrix} V_d \\ V_q \\ V_0 \end{bmatrix} = \frac{\sqrt{2}}{\sqrt{3}} \begin{bmatrix} \cos(\omega t) \\ \sin(\omega t) \\ 0 \end{bmatrix}, \quad (2)$$

$$\sin(\omega t - \Theta) \approx (\omega t - \Theta). \quad (3)$$

In the proposed control strategy, there are two loops: the current control loop and the voltage control loop implemented in the design for synchronization of AAC with the grid to generate proper switching pulses for IGBTs in AAC.

The current and the voltage controllers used in the loops are implemented to control the static errors which can be reduced to bring the dq voltages and currents in steady state. The placement of the controllers is decided by the processing

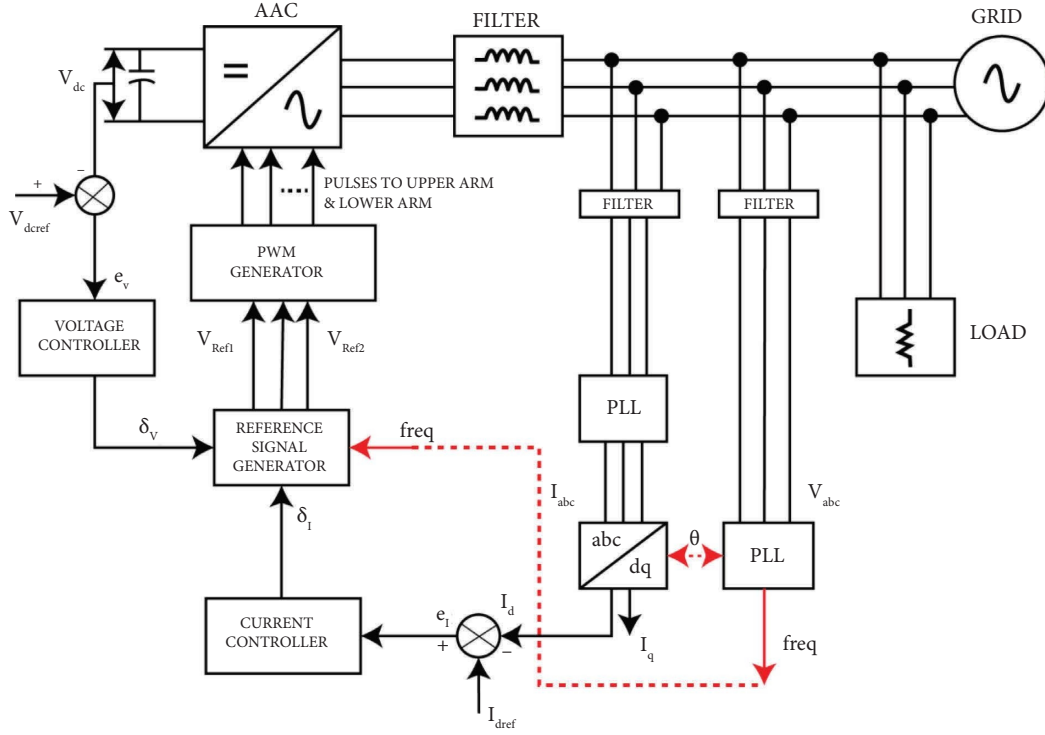


FIGURE 3: Block diagram of proposed control strategy.

speed and how quick they respond to signals [11]. The framework of the current control loop is presented in Figure 4.

In case of current loop, the controlling variables are inductor currents and in voltage control loop, capacitor voltages are considered as the controlling variables [11, 12]. The voltage control loop is used to maintain and regulate the real and reactive power. As the output voltage and current of AAC are 3 phases, it is complex and difficult to analyse. Thus, a synchronous reference frame PLL is an ideal control strategy that can be incorporated to provide the suitable synchronization where park transformation is necessary to track the phase angle of the output voltage of AAC and the AC grid. The AAC output voltage and current are the inputs to the PLL as shown in Figures 4 and 5. So, park transformation is applied to all the controllable variables such as currents and voltages as the phase angle of the AAC voltage must be decoupled in order to make the controlled current and grid voltage in phase with each other after filtering. The three-phase reference and the measured signals are transformed. This analysis is done as it is easy to control these constant dc values when transformed from abc to dq [9–16].

The PLL present in the current loop produces a controlling signal  $I_{(d-q)}$ , and the reference signal  $I_{dref}$  is compared with  $I_d$  to produce an error output signal  $e_i$  which is expressed by equation (4). In a rotating reference frame, the  $I_q$  component becomes zero when the PLL is locked, and when it is not locked, it exhibits a small error in case of a balanced three-phase system. A control/reference signal ( $V_{ref1}$ )  $\delta I$  which is given as input to the reference signal

generator is generated by the controller when the error signal  $e_i$  is fed to the controller. In case of the voltage control loop, the actual input voltage ( $V_{dc}$ ) given to AAC from the energy sources is measured and then compared with the desired reference voltage to produce an error signal  $e_v$  which is processed by the controller to generate a control signal  $\delta V$  which is fed to the reference signal generator which is expressed in equations (5). The framework of voltage control loop is depicted in Figure 6. In order to synchronize the AAC output voltage with the grid, the measured output voltage ( $V_{AACmeasured}$ ) is filtered and applied to the PLL for transformation to obtain the frequency and phase angle. The reference signal generator generates 3 phase voltages ( $V_1$ ,  $V_2$ , and  $V_3$ ) with the help of  $\delta I$  ( $V_{ref1}$ ),  $\delta V$ , and frequency of the measured output voltage which is presented in equations (6)–(11). The signals obtained from the reference signal generator ( $V_{referencea}$ ,  $V_{referenceb}$ , and  $V_{referencec}$ ) are then multiplied with  $\delta I$  ( $V_{ref1}$ ) to provide  $V_{abref}$  ( $V_{refa}$ ,  $V_{refb}$ , and  $V_{refc}$ ) signals. These signals are then used to generate pulses to trigger the IGBT switches in the submodules and DSs of AAC by comparing with a carrier signal using the phase shift PWM technique in a proper manner to achieve the desired output which is represented by equations (12)–(14). The flow and modules for generating the reference signals and switching pulses to AAC are represented in Figure 6.

$$I_{dref} - I_d = e_i, \quad (4)$$

$$V_{dc} - V_{dc} = e_v, \quad (5)$$

$$V_1 = \sin\left(2\pi ft + \frac{\pi}{2} - \delta V\right), \quad (6)$$

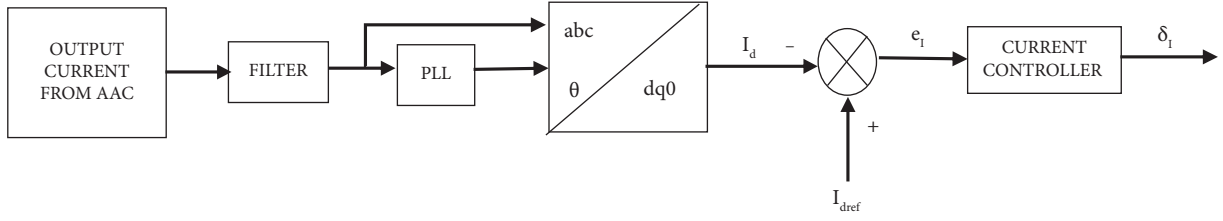


FIGURE 4: Framework of the current control loop.

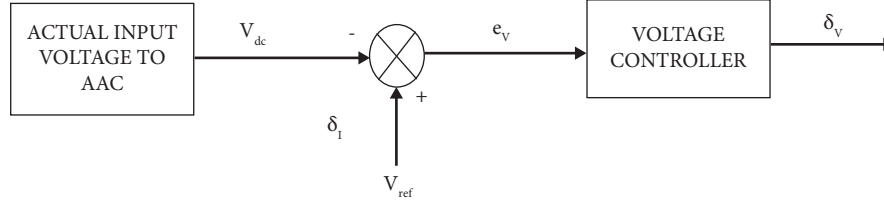


FIGURE 5: Framework of the voltage control loop.

$$V_2 = \sin\left(2\pi ft + \left(2 * \frac{\pi}{3}\right) + \frac{\pi}{2} - \delta V\right), \quad (7)$$

$$V_3 = \sin\left(2\pi ft + \left(4 * \frac{\pi}{3}\right) + \frac{\pi}{2} - \delta V\right), \quad (8)$$

$$V_{referencea} = \delta I * V_1, \quad (9)$$

$$V_{referenceb} = \delta I * V_2, \quad (10)$$

$$V_{referencec} = \delta I * V_3, \quad (11)$$

$$V_{refb} = V_{referenceb} * \delta I, \quad (12)$$

$$V_{refc} = V_{referencec} * \delta I, \quad (13)$$

$$V_{refc} = V_{referencec} * \delta I. \quad (14)$$

(1) *Controllers.* There are innumerable controllers available and still research is on progress to invent efficient, optimal, and high-speed controllers which can be implemented in the control systems to achieve the desired output depending on various applications. In this paper, three different controllers such as the conventional PID, fractional order proportional integral derivative (FOPID), and the FOPID controller trained by the metaheuristic algorithm is incorporated in the proposed control strategy to obtain the desired output of AAC, and a comparative analysis is done based on the performance and the THD value of the output voltage.

The PID controller is a versatile and robust feedback controller used in numerous applications. It is sometimes referred to as the three-mode controller (or three-term controller) because it has three parameters in its design. The value of these parameters is determined based on the performance index. When the system parameters are altered

to the point where the index reaches an extreme value, typically a minimum value, the system is said to have attained optimal control. The performance index may be either positive or zero and is determined using the expressions such as integral square error (ISE), integral absolute error (IAE), integral time squared error (ITSE), and integral time absolute error (ITAE) which are functions of the error signal.

In  $s$ -domain, the transfer function of PID controller is given by

$$G(s) = \frac{U(s)}{E(s)} = K_p + K_i \frac{1}{s} + K_d s, \quad (15)$$

where  $G(s)$  is the plant transfer function,  $U(s)$  and  $E(s)$  are output and input signals to the PID controller, and  $K_p$ ,  $K_i$ , and  $K_d$  are the proportional, integral, and differential gain parameters [17].

Even though PID controllers are suitable widely for all industrial applications, only a partial part of the loops in the PID controllers is tuned to achieve the optimum result. The extension of study of derivatives and integrals for noninteger orders led to the latest advancement in the mathematical analysis which paved path for fractional calculus [18] which caused a transition from classical models designed by differential equations for noninteger order. The fractional calculus has been used in recent years to model and control a variety of physical systems, diverse and widespread fields of engineering and science applications in order to increase the quality and robustness of the conventional PID controller which led to the implementation of fractional order PID (FOPID) controllers in control systems fractional-order controllers with fractional orders of  $I$  and  $D$  is one of the techniques used to enhance conventional PID controllers. FOPID controllers have two additional parameters, the order of fractional integration and the order of fractional derivative, in addition to the proportional, integral, and derivative parameters ( $K_p$ ,  $K_i$ , and  $K_d$ ) as shown in Figure 7. In order to increase the FOPID's flexibility, it has five

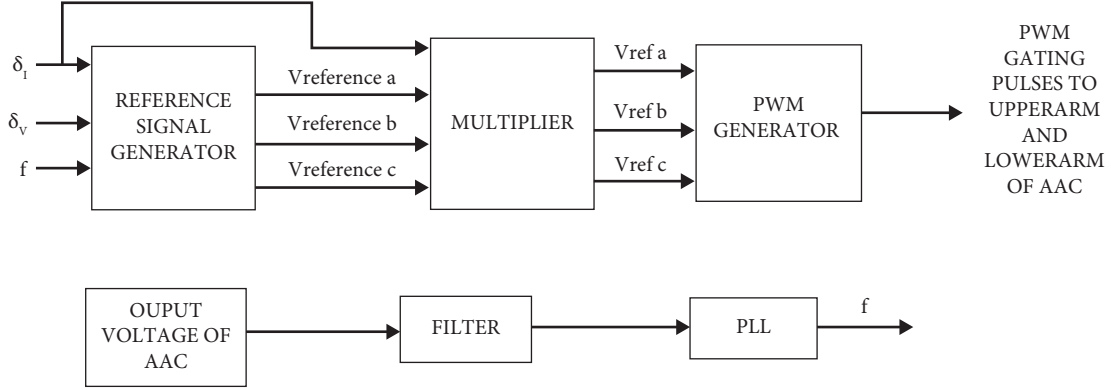


FIGURE 6: Block diagram of generation of PWM gating pulses to upper and lower arm of AAC.

parameters which have the freedom to tune over a wide range to obtain an accurate output [18–21].

The design of FOPID controller is very complex as it contains additional two variables ( $\lambda$ ,  $\mu$ ) to obtain a good performance of the system. The FOPID differential equation is given by the following equation:

$$U(s) = \left( K_p + \frac{K_i}{s^\lambda} + K_d s^\mu \right) E(s), \quad (16a)$$

where  $G(s)$  is the plant transfer function,  $K_p$ ,  $K_i$ ,  $K_d$ ,  $\lambda$ , and  $\mu$  are the proportional, integral, and differential gain, the order of fractional integration, and the order of fractional derivative parameters. The FOPID differential equation is given by the following equation:

$$U(t) = K_p E(t) + K_i D^{-\lambda} E(t) + K_d D^\mu E(t), \quad (16b)$$

where  $U(t)$  is the command signal given to the plant to achieve the desired output,  $E(t)$  is the error signal which is the difference between the set point/reference point and the actual or measured output, and  $D$  is the functioning operator related to the order of differential and integral.

**2.4. Bacteria Foraging Optimization Algorithm.** The bacteria foraging algorithm, a novel nature-inspired optimization technique, is based on how a swarm of *Escherichia coli* forages collectively. The four basic processes that make up the optimization process are chemotaxis, swarming, reproduction, and elimination-dispersal. These procedure particular and theoretical underpinnings are both discussed.

Animals that use ineffective foraging strategies are eliminated by natural selection (the means of finding, handling, and consuming food). This strategy thereby encourages the genetic transfer of the animal efficient foraging strategies. Better food-seeking organisms can successfully reproduce, whereas those with lower reproductive success rates are either wiped out or altered. The BFOA feeds similarly to the *E. coli* bacteria that dwell in our intestines. This technique has successfully shown its efficiency as a tool for power system optimization [22, 23]. Following is a brief discussion of the four stages of the

foraging process: chemotaxis, swarming, reproduction, and elimination.

**2.4.1. Chemotaxis.** Figure 8 shows how the chemotherapeutic taxis mimic the swimming and tumbling motions of *E. coli*. Moving in the same direction continually is a requirement of swimming. While tumbling is characterised by irregular movement within a stride, it depends on how the nutrients were found along the way. As their health improves, bacteria will continue to travel in that way. However, if there is a deadly material nearby, it will fall or veer off course. Throughout its existence, the bacteria will shift between the two states. The movement of *E. coli* bacteria throughout a search area for a nutrient is described by the following equation:

$$\theta^n(i+1, j, k) = \theta^n(i, j, k) + C(n) \cdot \varphi(i), \quad (17)$$

where  $C(n)$  indicates the count of steps moved by bacteria randomly represented by tumble process,  $\varphi(i)$  represents the tumble generating a unit length randomly, and  $\theta^n$  represents the position of the  $n$ th bacterium at the  $i$ th chemotactic,  $j$ th reproduction steps, and  $k$ th elimination dispersal event [24].

**2.4.2. Swarming.** Germs move forward in concentric circles due to the phenomenon known as swarming. Due to the nutritional impact, it will be split using succinate into small groups. Bacteria under duress produce attractants that signal other bacteria to form a swarm. To warn others to remain at a safe distance from it, it also produces a repellent. They are all drawn to one another by the attractant and drawn away from one another by the repellent as a result.

**2.4.3. Reproduction.** According to the most fundamental principle of natural selection, the healthiest bacteria will reproduce in this environment, which is how bacteria replenish their numbers. They will replace any undesirable or defunct microorganisms. The population remains unaltered as a result. The replications of the healthiest bacteria were

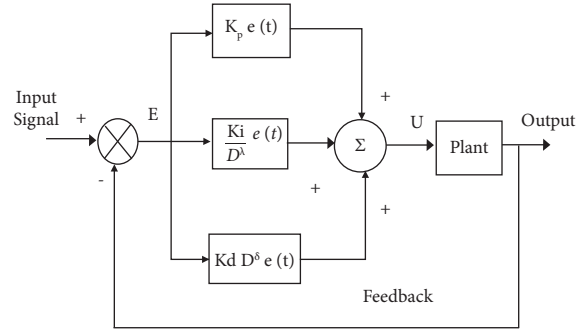


FIGURE 7: Block diagram of FOPID controller.

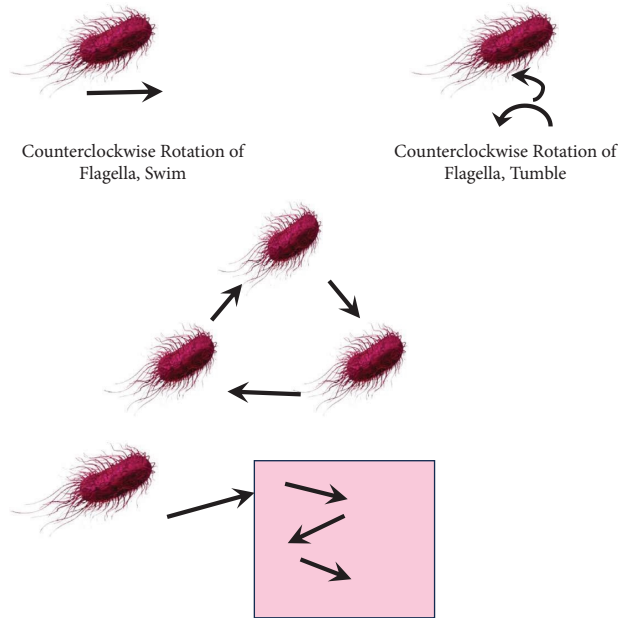


FIGURE 8: Chemotaxis process of BFOA.

placed in the same area as the original (unchanged). The stronger, healthier microorganisms frequently die off. The healthiest bacteria will eventually create its own generation with the identical copy, regardless of gender.

**2.4.4. Elimination.** The unfavourable environmental conditions will influence the bacteria's daily survival, or they will eventually move to the ecosystem's healthiest area. This is a natural phenomenon where the bulk of the germs disperse randomly in all directions as a result of an abrupt change in the environment. Even in the direst situations, all the bacteria in one region can move to another. In this new location, the bacteria can now find the global optimum. Furthermore, it might help bacteria get away from the local optima's trap. Figure 9 depicts the suggested BFOA algorithm's flow diagram.

The main objective of this work is to achieve a low harmonics output AC voltage and current across the AAC. In order to obtain the goal, a FOPID controller tuned with BFOA is incorporated in the feedback loop of the control strategy, and the design is implemented using MATLAB

software. The FOPID controller tuned by BFOA performance is estimated by the performance indices which are based on the error criterion. There are many performance criterions to maximize and minimize the desired parameters. In this paper, the integral absolute error (IAE) is implemented to achieve the desired AC output voltage and current. The generalised IAE is given in the following equation:

$$\text{IAE} = \int_0^t |e^t| dt, \quad (18)$$

where  $e^t$  is the error of the signal.

In Figure 3, there are two control loops in the control strategy where two FOPID controllers trained by bacterial foraging optimization algorithm are designed to achieve the desired AC output voltage and current.

The objective function of output current control and output voltage control is given by equations (4) and (5). The differential equations of the FOPID controllers can be expressed by the following equations:



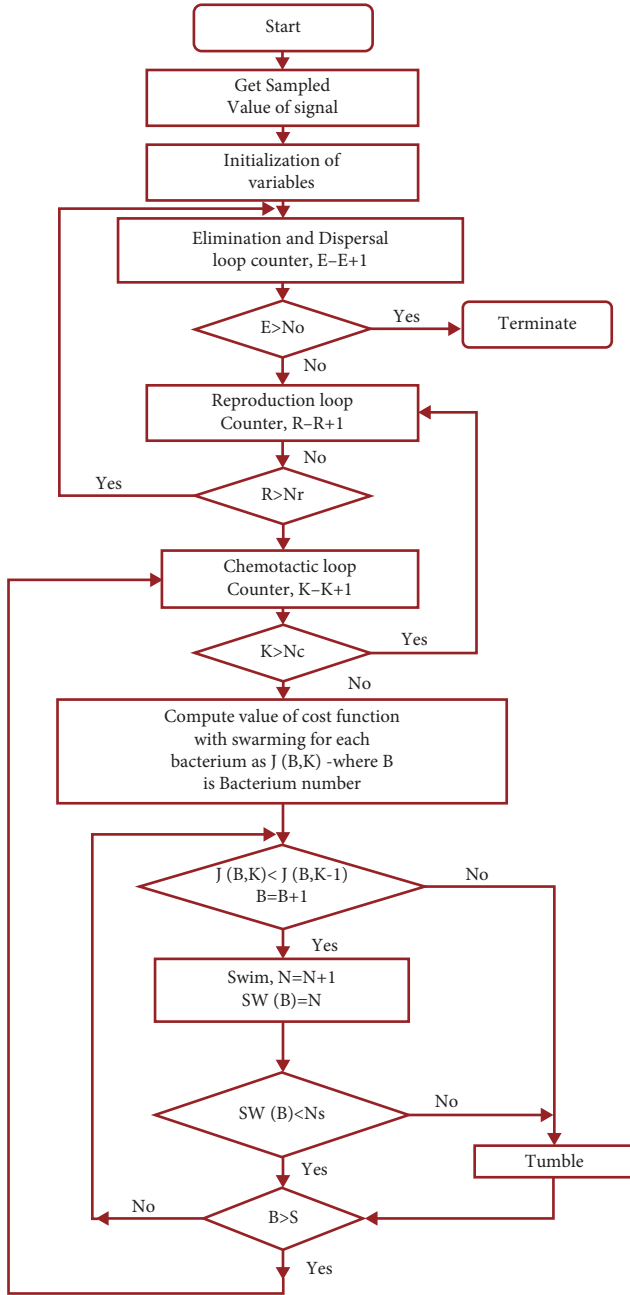


FIGURE 9: Flow diagram of BFOA.

$$\delta I(t) = K_p \cdot eI(t) + K_i \cdot D^{-\lambda} \cdot eI(t) + K_d \cdot D^{\mu} \cdot eI(t), \quad (19a)$$

$$\delta V(t) = K_p \cdot eV(t) + K_i \cdot D^{-\lambda} \cdot eV(t) + K_d \cdot D^{\mu} \cdot eV(t), \quad (19b)$$

where  $\delta I(t)$  and  $\delta V(t)$  are the controlling signals to generate the three-phase sinusoidal reference signals. The phase shift PWM technique is used to generate the pulses for firing the gates of the IGBT switches in the AAC to achieve the desired output voltage and current [25, 26].

The BFOA consists of four processes in order to achieve its prey. They are (1) chemotaxis, (2) swarming, (3) reproduction, elimination, and dispersal process. The BFOA is a process of iteration which begins by initializing the population (prey food) which in this case is to compute the voltage error  $eV(t)$  and current error  $eI(t)$ . The following is the procedure implementation of BFOA:

*Step 1. Parameter initialization*

- $n$ : dimension of the search space
- $S$ : number of bacterium (population size)
- $N_c$ : chemotactic steps
- $N_s$ : swim steps
- $N_{re}$ : reproduction steps
- $N_{ed}$ : elimination and dispersal steps
- $P_{ed}$ : probability of elimination

$C(i)$ : step size

*Step 2. Bacteria and parameters initialization*

- (i) Initialize the population of bacteria with random positions in the search space.
- (ii) Initialize parameters:
  - (iii) Chemotactic steps ( $N_c$ ) = [value]
  - (iv) Swim steps ( $N_s$ ) = [value]
  - (v) Reproduction steps ( $N_{re}$ ) = [value]
  - (vi) Elimination-dispersal steps ( $N_{ed}$ ) = [value]
  - (vi) Probability of elimination ( $P_{ed}$ ) = [value]
  - (viii) Initial step size ( $C(i)_{initial}$ ) = [value]

*Step 3. Iterate through chemotaxis, swarming, reproduction, and elimination-dispersal for each bacterium  $i$  in the population,*

- (i) Perform chemotaxis:
- (ii) Compute the fitness function  $F(i)$  based on IAE using the current controller parameters.
- (iii) Update bacterium's position based on chemotactic steps and step size:  $x(i, t+1) = x(i, t) + C(i) \cdot \text{current} \cdot \text{random\_vector}()$
- (iv) Perform swarming:
- (v) Determine the best bacterium  $j$  in the neighborhood of bacterium  $i$ .
- (vi) Update bacterium's position toward the best bacterium:  $x(i, t+1) = x(i, t+1) + \text{random\_vector}() \cdot (x(j, t) - x(i, t+1))$
- (vii) Perform Reproduction:
  - (viii) Generate a new bacterium based on the current bacterium's position and fitness.
  - (ix) The new bacterium's position is perturbed by a small random vector.
  - (x) Perform elimination-dispersal:
  - (xi) With probability  $p_{ed}$ , eliminate bacterium  $i$  from the population.

- (xii) Replace eliminated bacteria with new randomly initialized bacteria.

*Step 4.* Update controller parameters

- (i) Update the controller parameters:
  - (ii) Proportional gain  $(K_p) = K_p + C(i)_{\text{current}} * \text{random\_vector}()$
  - (iii) Integral gain  $(K_i) = K_i + C(i)_{\text{current}} * \text{random\_vector}()$
  - (iv) Derivative gain  $(K_d) = K_d + C(i)_{\text{current}} * \text{random\_vector}()$
- (v) Fractional orders:
  - (vi)  $\lambda = \lambda + C(i)_{\text{current}} * \text{random\_vector}()$
  - (vii)  $\mu = \mu + C(i)_{\text{current}} * \text{random\_vector}()$

*Step 5.* Controller performance evaluation

- (i) Evaluate the controller's performance using IAE with the updated parameters.
- (ii) Repeat the iterations until a stopping criterion is met.

*Step 6.* Implementation and testing

- (i) Implement the FOPID controllers with the updated parameters in MATLAB.
- (ii) Simulate and test the control strategy with the AAC system model to observe the impact of the tuned FOPID controllers.

*Step 7.* Analysis and results

- (i) Analyse simulation results to assess the effectiveness of the tuned FOPID controllers in achieving low harmonics AC output voltage and current.

*Step 8.* Conclusion

- (i) Summarize the results and findings, discussing the effectiveness of the proposed control strategy for achieving low harmonics AC output voltage and current in the AAC system.

*2.5. Comparative Analysis of PID, FOPID, and FOPID-BFOA Controllers.* A comparative analysis on the performance of a nine-level AAC using controllers such as PID, FOPID, and FOPID controller using bacteria foraging optimization technique that are implemented in the proposed control strategy to obtain the desired output and also its fast Fourier transform (FFT) spectral analysis is designed and simulated in MATLAB/Simulink for the configuration which is depicted in Figure 3. The Ziggler Nicholas method, Cohen-Coon, Astrom-Hagglund (AMIGO) and Chien-Hrones-Reswick methods are the different tuning methods that are available for determining the parameters for the designing of the PID and FOPID controllers [19–21]. The PID and FOPID controllers can also be tuned either manually or automatically by the tuner in MATLAB/Simulink.

There are many metaheuristic algorithms/techniques which have been implemented in research for optimization of various parameters depending upon the applications since many years, and it has gained more importance in control

systems because it can provide the best solution among various other possible solutions for any given complex problem optimally and quickly. To obtain a smooth and regulated AAC output voltage, the values of  $K_p$ ,  $K_i$ ,  $K_d$ ,  $\lambda$  and  $\mu$  are obtained by tuning the FOPID controller using the bacteria foraging optimization algorithm (FOPID-BFOA) to achieve the optimized desired values. The design parameters of  $K_p$ ,  $K_i$ ,  $K_d$ ,  $\lambda$ , and  $\mu$  used in PID, FOPID, and FOPID-tuned BFOA controllers are tabulated and presented in Table 1.

Thus, on performing the comparative analysis of PID, FOPID, and FOPID-tuned BFOA, it is analysed that error value obtained by FOPID-tuned BFOA is very less when compared to other controllers. The spectral analysis is also determined for the AAC output voltage which gives a THD value of 21.46% for the PID controller, 18.60% for FOPID, and 4.26% for FOPID-BFOA is shown in Figures 10 and 11. Thus, from the above analysis, it is found that FOPID-BFOA gives better results than other controllers.

### 3. The Proposed Energy Management System (EMS)

Due to the irregular availability of natural resources and climatic conditions, the renewable energy sources are insufficient to deliver power to meet the load requirements without any interruption which led to the inclusion of energy storage devices. In order to prevent any supply interruption or for erratic or unexpected load consumption, energy storage is therefore a crucial component of a hybrid renewable energy system.

When there is more energy generation than load demand, the energy storage system stores the excess energy and delivers it when there is more load demand than energy generation. By correcting any discrepancies between energy demand and supply, energy storage also serves as an energy buffer, enhancing system functionality and reducing the impact of any power outages. In this topology, battery banks act as a backup to meet the demand. The entire power flow is managed, self-controlled and regulated by a controller to decide and give priority to which energy source has to fulfil the load demand based on the availability and charging/discharging the battery depending on the state of charge (SoC) and isolate the load from the grid during conditions when the load demand is fulfilled by the microgrid. When the power from the solar, wind, and battery is not meeting up with the instantaneous load demand, then the controller immediately directs the grid to feed the load, thereby isolating the AAC side connected to microgrid.

The entire configuration of the proposed energy management system in integrating the microgrid, AAC, and the grid feeding an industrial load and a resistive load is pictorially represented in Figure 12. An efficient and optimal control strategy for utilising the renewable resources, energy storage device and charging/discharging of battery maintaining the uninterrupted power flow to meet the load demand is designed. The energy management system comprises of a controller which is programmed to perform the function of regulating and managing the energy from the renewable

TABLE 1: Design parameters of PID, FOPID, and FOPID-BFOA controllers.

Method	Parameter	Kp	Ki	Kd	$\mu$	$\lambda$	Error value
PID	Voltage	0.05672	0.95321	0.054787	—	—	12.894785
	Current	1.000	1.000	1.000	—	—	
FOPID (without optimization technique)	Voltage	4.535	0.908	3.276	0.282	0.420	10.224184
	Current	1.000	1.000	2.861	1.000	0.245	
FOPID-tuned bacteria foraging optimization technique	Voltage	0.022768	0.72301	0.3757	0.41266	0.94429	1.452902
	Current	1.000	1.000	7.937	1.000	0.300	

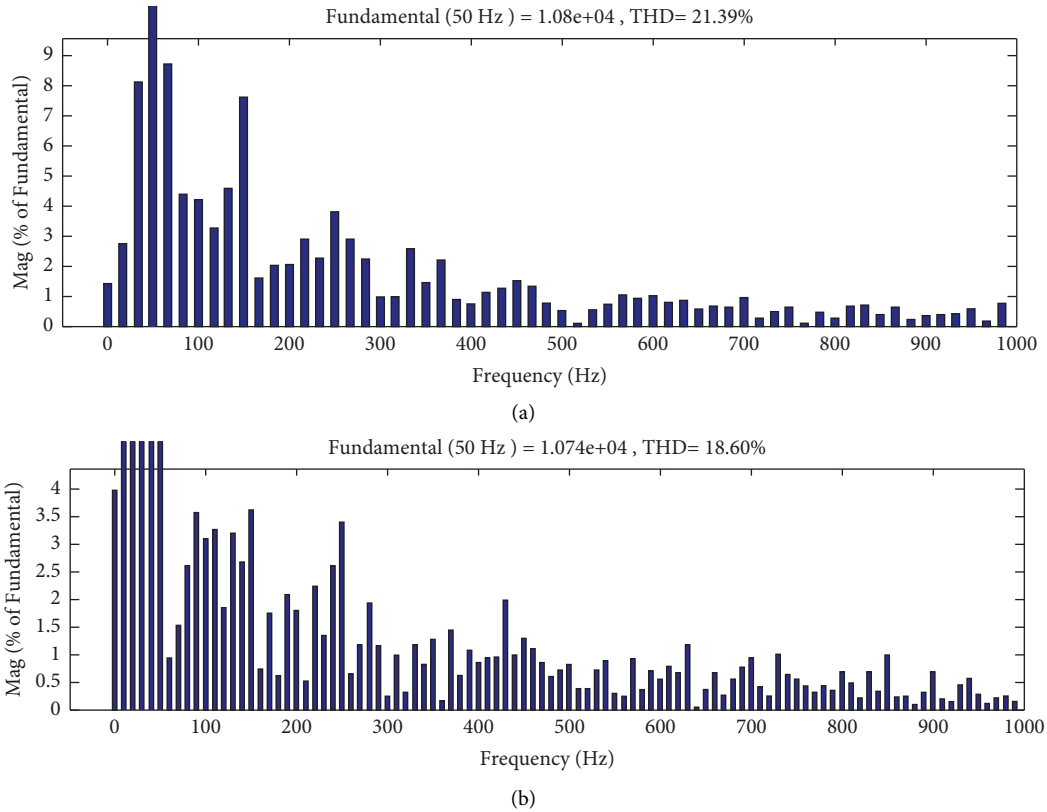


FIGURE 10: Spectral analysis of (a) PID controller and (b) fractional order PID controller.

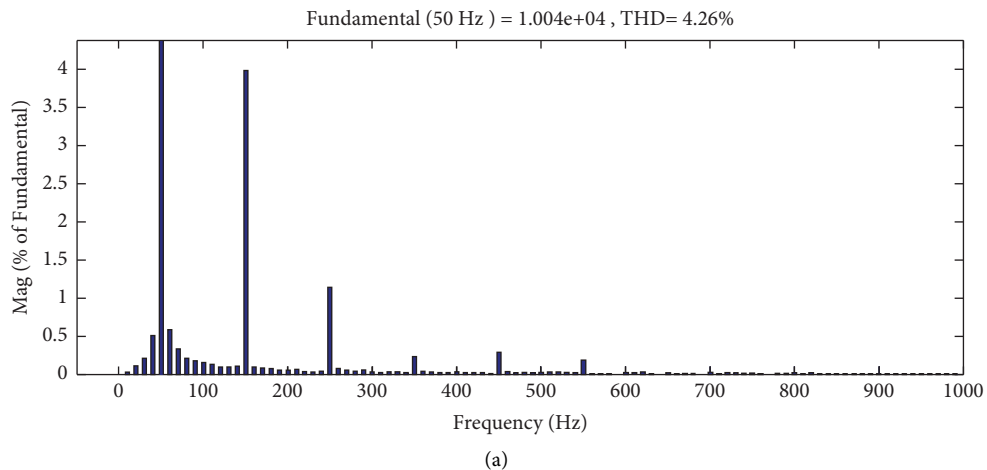


FIGURE 11: Continued.

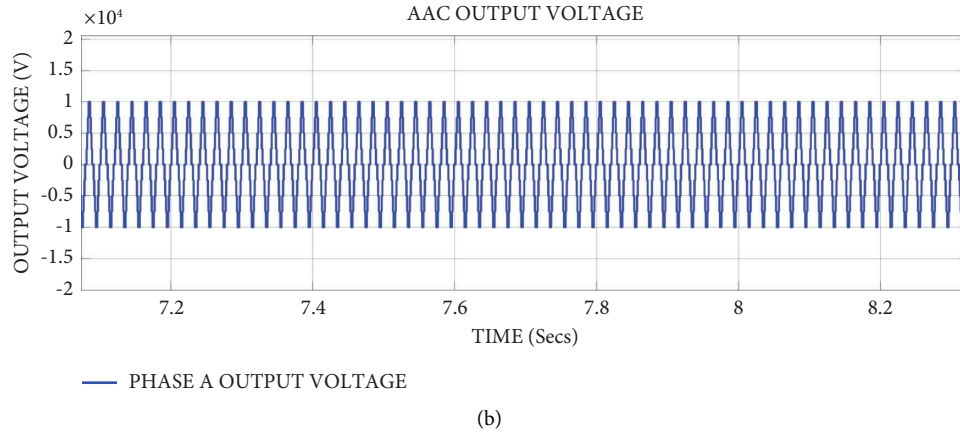


FIGURE 11: (a) Spectral analysis of FOPID controller tuned bacterial foraging optimization algorithm and (b) output voltage of nine-level AAC.

energy sources, from battery based on availability and economic sources or from the grid to be fed based on the instantaneous load demand requirements [27]. The controller receives the instantaneous power from solar, wind, battery and load and generates duty cycles (control signals/pulses) based on the availability of the input energy sources to maintain the power flow to the load. The AAC input voltage is being controlled by the control signals directed by the energy management controller whether the load is supplied either from renewable energy sources or battery. The battery is charged from the AC grid through an AC-DC converter when the grid is isolated from the load. A controlled and regulated 10 kV is achieved by the fuzzy controller implemented in the battery submodule to feed the AAC in case of renewable energy sources are unfavourable to generate power.

The input voltage to AAC is obtained either from the integrated CUK-SEPIC converter or from the battery. A three-phase output voltage of 10 kV is generated based on the switching pattern of the upper arm and lower arm submodules in each phase or leg. At the point of common coupling (PCC), the AAC and AC grid feeds the power to meet the load demand of an industrial and resistive load without any interruption. Based on the availability of power generated by renewable energy sources and battery, the AAC satisfies the load demand. But there are consequences which arise due to climatic factors/conditions which reduce the generation of power from them. The load demand is met without any interruption either from microgrid or AC grid by a control signal generated by the energy management controller. Thus, the energy management controller tracks the entire operating characteristics of all the devices and commands them to operate in a sequential manner to achieve an efficient way of integrating the microgrid and grid with the load without any discrepancies.

**3.1. Working Principle of the Integrated CUK-SEPIC DC-DC Converter.** The parameters such as voltage, current, and power obtained at the output of the solar PV system, wind turbine (after AC-DC conversion), and battery are not in a controlled and regulated form. So, it has necessitated the

inclusion of DC-DC converters to obtain a regulated output across the load. DC-DC converters play a vital role in the integration of microgrid with the AC grid.

In this proposed design, an integrated CUK-SEPIC DC-DC converter which is a dual-input converter has been incorporated. The integrated dual-input DC-DC converters have gained more importance in the latest power electronics applications in obtaining the converter output power based on the availability of the inputs. The main advantage of utilising the fused converters is that it reduces the number of devices used to build separate DC-DC converters allocated to operate separately for each input source voltage; this in turn reduces the cost and power losses and improves the efficiency of the converter [27–29].

The integrated CUK-SEPIC shown in Figure 13 operates based on the input energy sources availability. In this dual-input converter design, the CUK converter is connected to the solar PV system, and the SEPIC converter is connected to the wind turbines. LCUK, CCUK, M1, and D1 form the CUK converter circuit, and LSEPIC, CSEPIC, M2, and D2 frame the SEPIC converter. Lo and Co act as the filter and output is obtained across the common coupling terminals which are fed as input across AAC.

**3.1.1. Modes of Operation of an Integrated CUK-SEPIC DC-DC Converter.** The integrated CUK-SEPIC converter operates in two modes, and each mode has three switching states based on the availability of the inputs. In mode 1, if turn ON time for M1 is more when compared to M2, then the converter will operate in I, II, and IV switching states, and in mode 2, the converter will operate in I, III, and IV states [27–30]. Let us consider that  $ds_1$  and  $dw_1$  are the duty cycles of the solar PV system and wind system,  $I_s$  and  $I_w$  are the average and RMS input currents flowing from the solar PV system and wind system,  $V_{co}$  is the voltage across the output capacitor  $C_o$  and  $I_o$  and  $V_{oc}$  are the average output current and voltage of the converter at the point of common coupling. The output voltage at the point of common coupling is given by the following equation:

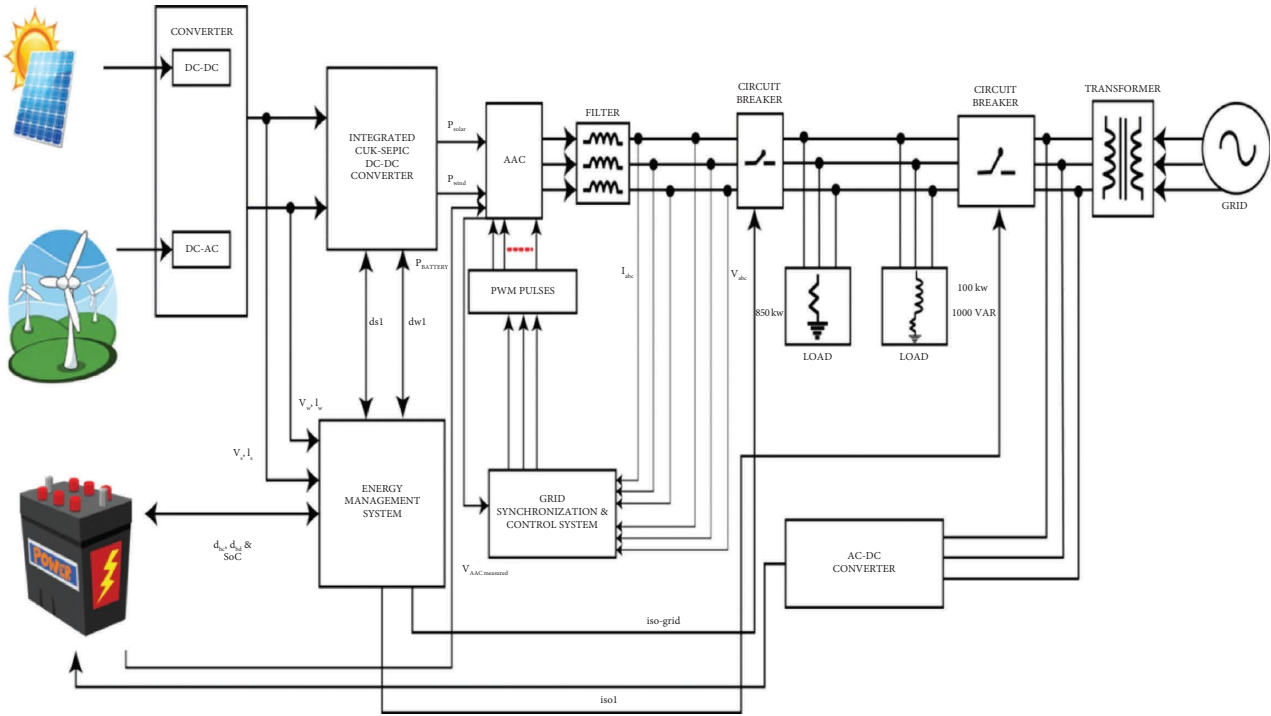


FIGURE 12: Block diagram of proposed energy management system.

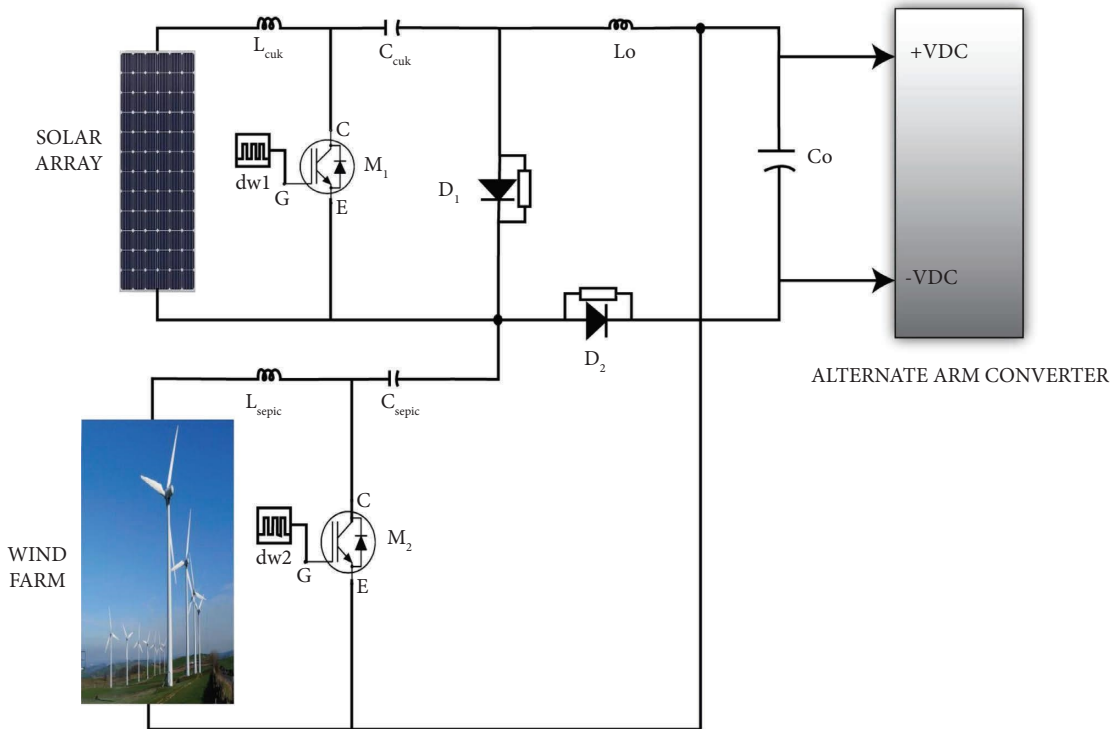


FIGURE 13: Circuit diagram of an integrated CUK-SEPIC DC-DC converter.

$$\mathbf{V}_o = \left( \frac{ds1}{1 - ds1} \right) \mathbf{V}_s + \left( \frac{dw1}{1 - dw1} \right) \mathbf{V}_w. \quad (20)$$

(1) *Mode 1. M1-ON and M2-ON.* In mode 1, both the solar and the wind outputs are available at the input of the converter. As both power generations are available, M1 and M2 are turned ON, and the diodes are reverse biased. The solar and wind voltages charge the inductors LCUK and LSEPIC. The output inductor  $L_o$  and output capacitor  $C_o$  are charged by the discharging currents of CCUK and CSEPIC. The energy stored in  $C_o$  appears across the point of common coupling which is fed as input to AAC. The relationship between the input and output parameters of the CUK-SEPIC converter is represented in the following equations:

$$\mathbf{I}_{Lcuk} = \mathbf{I}_s + \frac{V_s}{L_{cuk}} t; \quad 0 < t < ds1Ts, \quad (21)$$

$$\mathbf{I}_{Lsepic} = \mathbf{I}_w + \frac{V_w}{L_{sepic}} t; \quad 0 < t < ds1Ts, \quad (22)$$

$$\mathbf{I}_{L_o} = \mathbf{I}_o + \left( \frac{V_{cuk} + V_{sepic}}{L_o} \right) t; \quad 0 < t < ds1Ts, \quad (23)$$

(2) *Mode 2. M1-ON and M2-OFF.* The solar output is only active. So, M1 is switched ON and M2 is OFF. The diode D1 remains in reverse-biased condition, and the diode D2 becomes forward biased. The inductor LCUK stores energy due to solar input. The energy stored in CSEPIC discharges through D2 and charges LSEPIC. The capacitor CCUK discharges its energy and charges the inductor  $L_o$ , which in turn charges  $C_o$ . In this mode, the converter acts as a CUK converter. The relationship between the input and output parameters of the CUK-SEPIC converter is represented in the following equations:

$$\mathbf{V}_o = \mathbf{V}_s \left( \frac{ds1}{1 - ds1} \right). \quad (24)$$

(3) *Mode 3. M1-OFF and M2-ON.* The wind source is only active. In this mode, D1 is made forward biased, and D2 is reverse biased. The circuit operates as a SEPIC converter. The wind source charges the inductor LSEPIC, and as M2 is ON, the capacitor CCUK discharges through D1, thereby charging LCUK, and CSEPIC discharges its energy through M2, charging  $L_o$  and  $C_o$ . The relationship between the input and output parameters of the converter is represented in the following equations:

$$\mathbf{I}_{Lcuk} = \mathbf{I}_s + \frac{V_s - V_{cuk}}{L_{cuk}} t; \quad ds1Ts < t < dw1Ts, \quad (25)$$

$$\mathbf{I}_{Lsepic} = \mathbf{I}_w + \frac{V_w}{L_{sepic}} t; \quad ds1Ts < t < dw1Ts, \quad (26)$$

$$\mathbf{I}_{L_o} = \mathbf{I}_o + \left( \frac{V_{Co}}{L_o} \right) t; \quad ds1Ts < t < dw1Ts. \quad (27)$$

(4) *Mode 4. M1-OFF and M2-OFF.* In this mode, both solar and wind power generations are unavailable. Both the diodes D1 and D2 are forward biased; the inductors LCUK and LSEPIC discharge through D1 and D2 and so CCUK and CSEPIC start charging. During this condition, the inductor  $L_o$  discharges its stored energy through D1 and D2, thereby charging the capacitor  $C_o$ . The input and output parameters relationship of the converter is represented in the following equations:

$$\mathbf{I}_{Lcuk} = \mathbf{I}_s + \left( \frac{V_s - V_{cuk}}{L_{cuk}} \right) t; \quad dw1Ts < t < Ts, \quad (28)$$

$$\mathbf{I}_{Lsepic} = \mathbf{I}_w + \left( \frac{V_w - V_{Co} - V_{oc}}{L_{sepic}} \right) t; \quad dw1Ts < t < Ts, \quad (29)$$

$$\mathbf{I}_{L_o} = \mathbf{I}_o - \left( \frac{V_{Co}}{L_o} \right) t; \quad dw1Ts < t < Ts. \quad (30)$$

So, in this mode, no output voltage due to nonavailability of renewable energy sources at the input of the integrated CUK-SEPIC converter. So, a regulated output voltage is achieved across AAC to meet the load demand based on the renewable energy input sources availability.

*3.2. Behaviour of the Energy Management System.* The energy management system (EMS) plays a crucial role in controlling and regulating the power flow from various input energy sources to meet the load demand. The controller present in EMS receives input voltage and current from the solar PV system, wind, load, and battery. Depending upon the availability of input energy sources and to satisfy the load demand, the controller is programmed in such an efficient manner that it generates duty cycles (control signals)  $ds1$ ,  $dw1$ ,  $db1$ ,  $dbo1$ ,  $iso$ , and  $iso\_grid$  to direct the power from the solar PV system, wind mill, battery banks, and grid to meet the demand. The controller also commands over the charging/discharging of the battery. The energy management controller architecture [27] is depicted in Figure 14.

*3.3. Control Strategy of the Energy Management System.* The energy management system controller masters the operation of the integrated CUK-SEPIC converter, battery, AAC, and the AC grid to fulfil the requirements of the load by altering the duty cycles based on the availability and economic consideration of the input energy sources. In order to avoid any discrepancies in meeting the load demand, the controller is programmed such that it monitors and controls the entire system with the supporting slave controllers like fuzzy logic controllers in case of MPPT in solar PV system and wind system, to obtain the desired output across the point of common coupling at the outset of the integrated CUK-SEPIC converter, charging/discharging of battery depending on state of charge (SoC%) and FOPID-tuned BFOA controllers to achieve the desired output across AAC to synchronize with the grid and supply the load. The proposed energy management system flow diagram is presented in Figure 15.

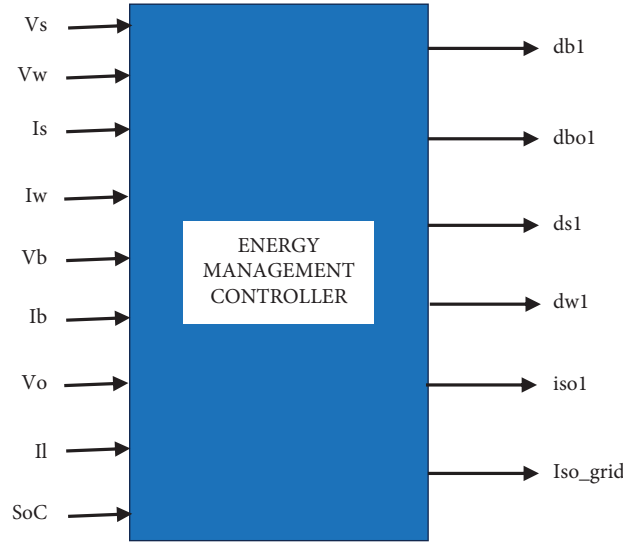


FIGURE 14: Architecture of the energy management controller.

The controller is programmed in such a way that it receives inputs from the solar PV system, wind system, battery, load, AAC, and the AC grid. The load current is compared by the controller with that of the solar and wind currents ( $I_s$  and  $I_w$ ) which is represented by the following equation:

$$I_s + I_w > I_L \quad (31)$$

The battery is charged to a maximum value of reference current  $I_{bchref}$  which is calculated by equation (32) which is the excess current and voltage available at the output of CUK-SEPIC converter at the point of common coupling.

$$I_{bchref} = (I_s + I_w) - I_L \quad (32)$$

The load is fed either from solar or wind or by both through the point of common coupling of the CUK-SEPIC converter and AAC depending on the duty cycles  $ds1$ ,  $dw1$ ,  $dbo1$ , and  $iso\_grid$ . The SoC of the battery and the direction of the current flowing through the battery are monitored by the controller. If the SoC is less than 10%, then the controller is programmed to regulate the duty cycles  $db1$ ,  $dbo1$ ,  $iso\_grid$ , and  $iso1$  and commands the AC grid to charge the battery till the battery current  $I_{bc}$  reaches the maximum value of reference charging current  $I_{bchref}$  or otherwise the battery voltage remains in the same voltage when  $I_{bc}$  is equal to  $I_{bchref}$  depending on the current flow direction through the battery and SoC. The increment or change in the duty cycle is represented by  $\Delta d$ . The load is fed from the output of AAC. When the power generation of solar and wind is less than the load demand, the load requirements are achieved by discharging of the battery accompanying the solar and wind power which is initiated by the duty cycles  $dbo1$  programmed by the controller when the SoC is greater than

40%. The battery will be discharged till  $I_{bdref}$  which is the maximum reference discharge current calculated as per the following equation:

$$I_{bdref} = I_L - (I_s + I_w) \quad (33)$$

Then, in the next case, if the load demand is neither satisfied by the renewable energy sources nor the energy storage devices, then the controller is programmed to change the duty cycles  $ds1$ ,  $dw1$ ,  $db1$ ,  $dbo1$ ,  $iso1$ , and  $iso\_grid$  in such a manner that the load is isolated from the input energy sources and AAC and the load requirements are fulfilled by connecting the load with the AC grid [30]. Thus, the controller which is embedded in the design of the energy management system optimizes and regulates the power flow between the microgrid, AAC, AC grid, and the load efficiently and quickly.

## 4. Design and Operation of EMS

*4.1. Selection of System Parameters.* The proposed integration of microgrid, AAC, and the grid, feeding an industrial load and a resistive load, along with an energy management system has been designed and analysed using MATLAB/Simulink software. The results are discussed in the next section in detail with waveforms in support for analysis.

The entire model has been designed using MATLAB/Simulink which comprises of a solar energy conversion system, wind energy conversion system, integrated CUK-SEPIC converters, battery, AAC, FOPID controller, grid, transformer, loads, and energy management controller to control and regulate the instantaneous power delivered by various energy sources to the load is shown in Figure 16.

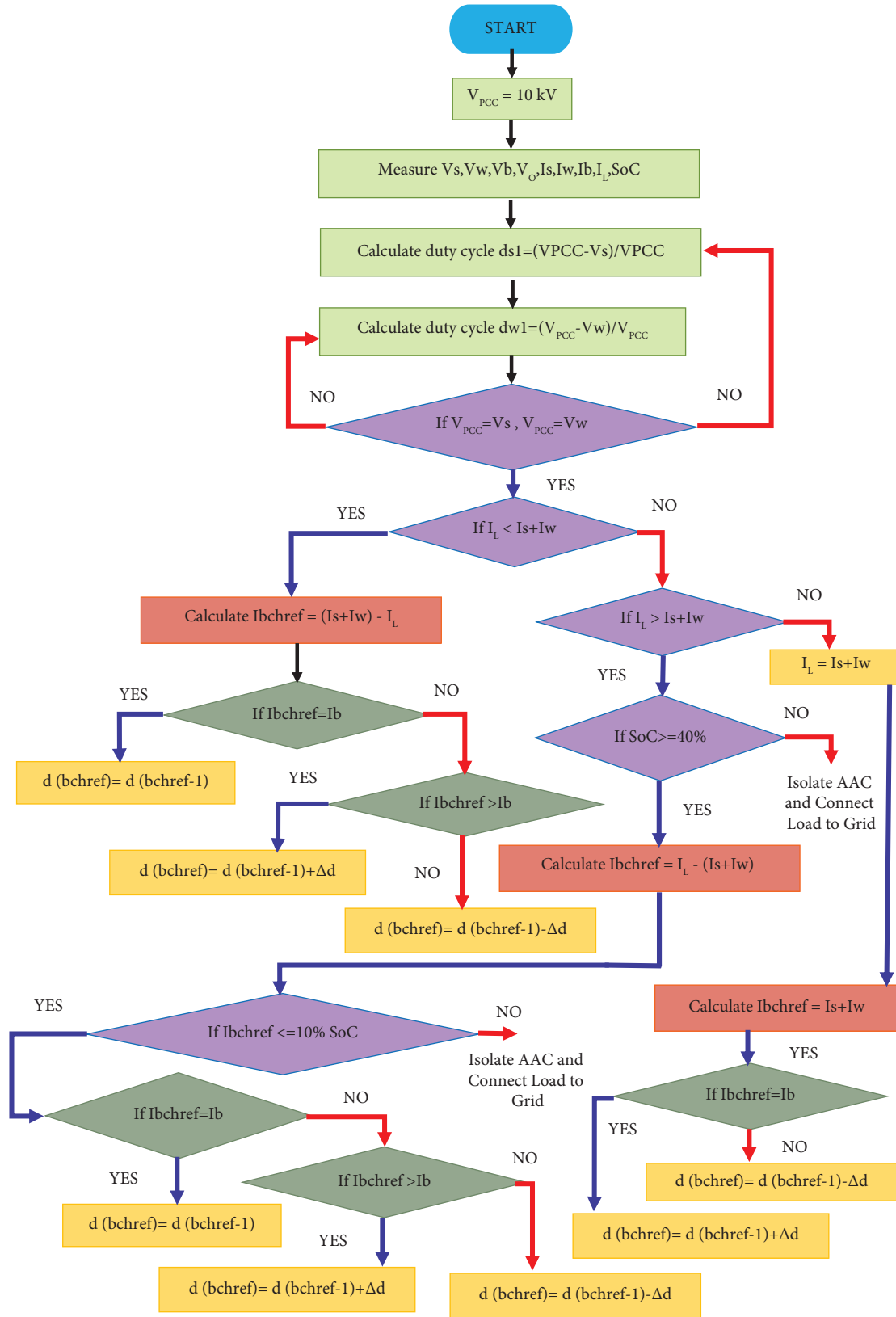


FIGURE 15: Flowchart of the proposed energy management system.



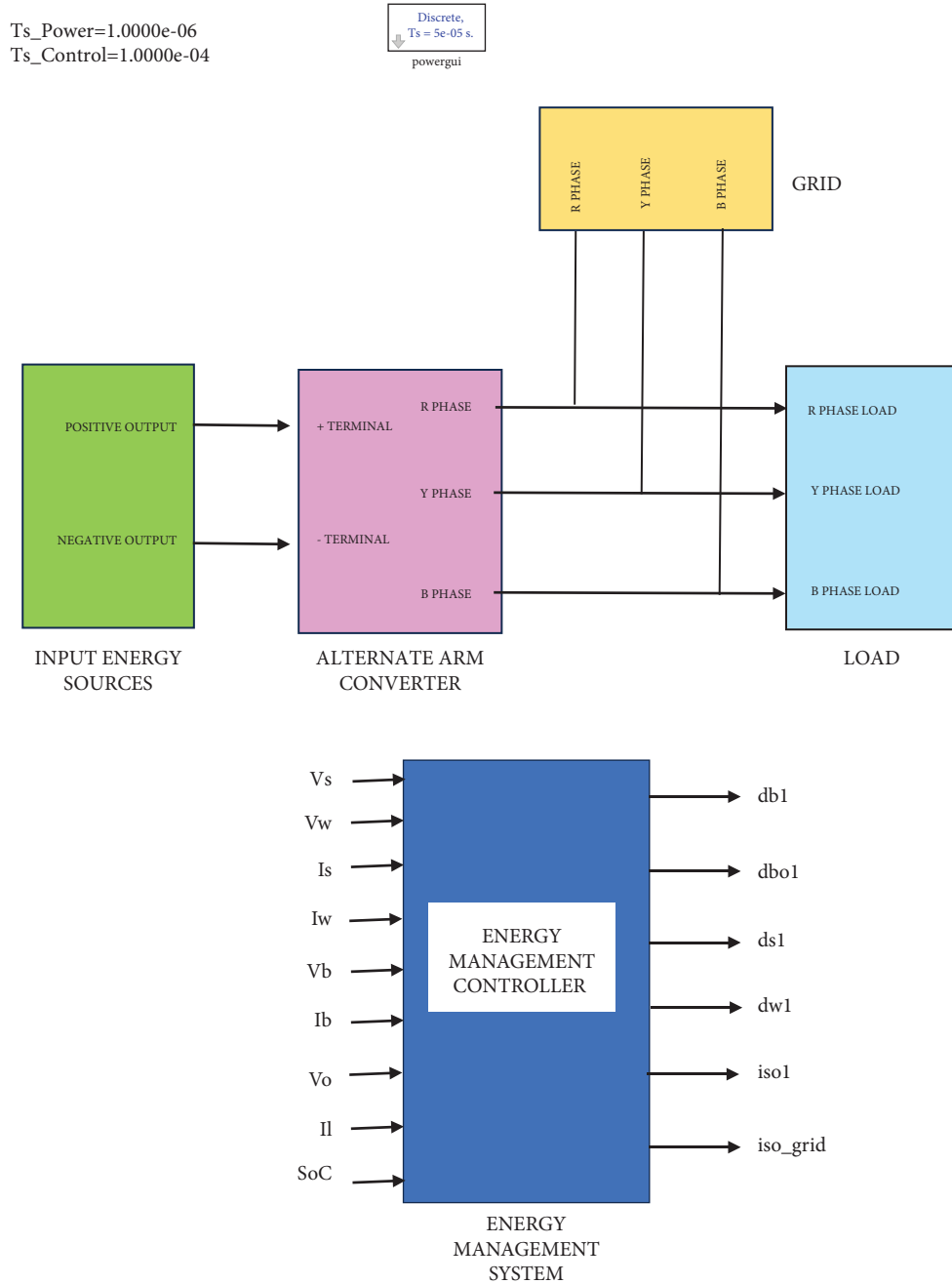


FIGURE 16: Design of the proposed energy management system.

A solar PV system is designed to generate a 10 kV output voltage. A solar module of  $1\text{ kW/m}^2$  with a voltage at MPPT ( $V_{mp}$ ) of 54.7V, current at MPPT ( $I_{mp}$ ) of 5.58A and maximum power rating of each module to be 305W is chosen to design the solar PV system. So, the design parameters for a 10kV solar PV system are calculated as follows:

Module specification for  $1\text{ kW/m}^2$  of  
 type: SunPower SPR-305-WHT  
 voltage: 54.7 V, current: 5.58 A and P: 305 W

For  $V_t = 10,000\text{ V}$ ,  
 $V_t = \text{No. of series-connected module per string} * 54.7\text{ V}$   
 no. of series-connected module per string =  $10,000 / 54.7 = 183$   
 total no. of modules = total no. of series connected modules per string \* no. of parallel strings  
 no. of parallel strings = 1500  
 total no. of modules =  $183 * 1500 = 2,74,500$   
 total power = total no. of modules \* power of one module =  $2,74,500 \times 305 = 83.7 \times 10^7\text{ W}$

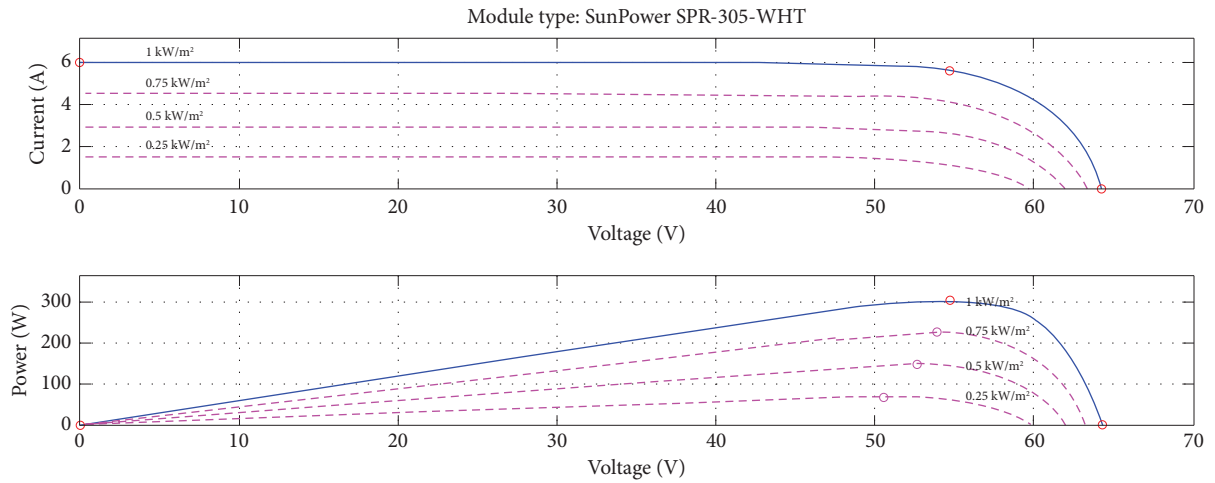


FIGURE 17: I-V and P-V characteristics of a single solar module.

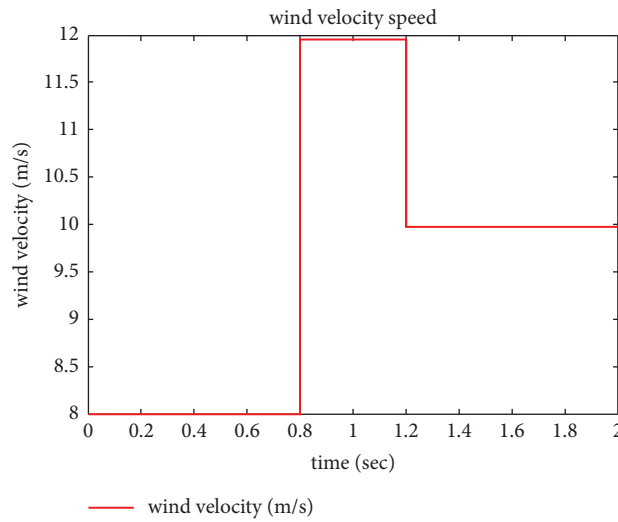


FIGURE 18: Wind speed of the wind turbine system.

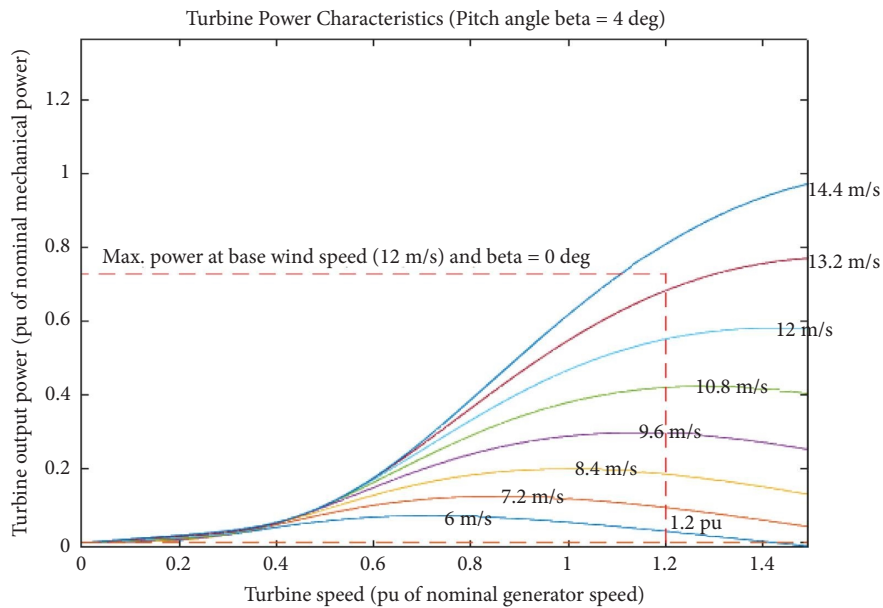


FIGURE 19: Wind turbine with pitch angle = 4 degrees.

So, solar PV system design parameters are chosen as number of cells per module: 96, number of series-connected modules per string: 183, and number of parallel strings: 1500

The I-V and P-V characteristics of a single solar module are represented in Figure 17. A wind farm with grid-tied wind turbine system is designed for a rated voltage of 10 kV, a variable wind speed of 8 m/s for a period of 0.8 seconds, 12 m/s from 0.8 seconds to 1.2 seconds and 10 m/s from 1.2 seconds to 2 seconds is chosen as the wind velocity for a power rating of 70 MW for analysis purpose is shown in Figures 18 and 19.

The instantaneous power generated by solar and wind systems are fed to the dual input integrated CUK-SEPIC converter. This topology has been a boon to the standalone and grid-tied systems, where the renewable energy sources are unpredictable and intermittent. The main purpose to introduce this integrated converter is to maintain and satisfy the load demand by either a solar PV system ( $V_s$ ) or a wind farm ( $V_w$ ) or from both the sources without any interruption. An integrated CUK-SEPIC DC-DC converter design parameters is presented in Table 2.

The duty cycles/control signals are  $ds_1$ ,  $dw_1$ ,  $db_1$ ,  $dbo_1$ ,  $iso_1$ , and  $iso\_grid$  generated by the energy management controller based on the input signals  $V_s$ ,  $V_w$ ,  $V_b$ ,  $V_o$ ,  $I_s$ ,  $I_w$ ,  $I_{bc}$ ,  $I_{bd}$ ,  $I_L$ , and SoC obtained from various energy sources and the load to regulate the flow of power between the input energy sources and the load rapidly without any interruption.

The output voltage of  $V_o = 10$  kV of the CUK-SEPIC converter is maintained by fuzzy logic controller using the following equations:

$$dso = \frac{V_o - V_s}{V_o}, \quad (34)$$

$$dwo = \frac{V_o - V_w}{V_o}, \quad (35)$$

where  $dso$  and  $dwo$  are duty cycles generated by fuzzy controller to achieve constant voltage across the common terminals of the CUK-SEPIC converter. The duty cycles  $ds_1$ ,  $dw_1$ ,  $dso$ , and  $dwo$  are compared, and two pulses are generated which are used to trigger the MOSFET/IGBT switches M1 and M2 in the CUK-SEPIC converter to generate the constant output voltage  $V_o$  at the point of common coupling output terminals of the converter. This constant output voltage is fed to the alternate arm converter to meet the load requirements.

The input to AAC is fed with a constant voltage of 10 kV either from the output obtained at the common coupling terminals of the integrated CUK-SEPIC converter or from the battery based on the duty cycles (control signals) given to the switches which control the input given to AAC. If the input to AAC must be fed from the solar PV system or wind farm, two interfacing switches will be triggered with the same duty cycle ( $db_1$ )

generated by the energy management controller; otherwise, if the output from the battery must be fed as input to AAC, another set of switches will be triggered by the duty cycle ( $db_1$ ). The battery is acting as an alternative reserve when there is no availability of power generated from the renewable energy resources. The battery type implemented in this design is nickel-metal hydride (NiMH). When compared to lead-acid, nickel-cadmium (Ni-Cd), and lithium-ion batteries, the NiMH batteries produce higher power and energy density with long life cycle. The state of charge (SoC%) of the battery does not affect the output power and they very safe in the point of operation and handling compatibility. But they are very expensive when compared to lead-acid battery [31, 32].

The discharging characteristics of the nickel-metal-hydride battery are represented in Figure 20. The battery discharges its voltage to AAC depending on the duty cycle  $db_1$  generated by the energy management controller. The AC grid charges the battery when the battery is not discharging the energy to AAC.

The parameters of the battery are given below:

Type: nickel-metal-hydride battery

Nominal voltage: 10500 V;

rated capacity (Ah): 5000;  $V_{in} = 9000$  to 10500 V;  
SoC = 50%

Battery response time: 0.01 seconds

The alternate arm converter is a HVDC topology. In this proposed design, AAC is used to interface the input energy sources and the load. A nine-level AAC is designed for a DC input voltage of 10 kV to be integrated for microgrid applications. The upper arm and lower arm inductors ( $L_{arm}$ ) and arm capacitors ( $C_{arm}$ ) are calculated using the following equations [6, 15, 33, 34]:

$$L_{arm} = \frac{1}{C_{arm} \omega^2} \frac{2(ha^2 - 1) + ma^2 ha^2}{8ha^2(ha^2 - 1)}, \quad (36)$$

$$C_{arm} = \frac{EP * S_n}{3V_{dc}^2}, \quad (37)$$

$$C_{arm} = \frac{C_{sm}}{n}, \quad (38)$$

where the modulation index ( $ma$ ) can be varied for under-modulation and over-modulation from 0 up to 1.15.  $ha$  is the harmonics,  $f$  is the fundamental frequency ( $f = 50$  Hz),  $\omega$  is the angular frequency in rad/s ( $\omega = 2 * \pi * 50$  Hz = 314.15 rad/s),  $S_n$  is the converter rated power, and  $EP$  is the energy power ratio. Choosing the  $EP$  value relies on the applications of the converter and it is usually chosen between 0 and 50 J/KVA. In this design,  $V_{dc}$  is the DC link input voltage to the converter.  $C_{SM}$  is the submodule capacitance, and  $n$  is the number of submodules in the upper arm and lower arm. The number of submodules in the arms is selected based on the output voltage levels.

TABLE 2: Design parameters of the integrated CUK-SEPIC DC-DC converter.

Input voltage 1 (Vs)	8500 V to 10000 V	
Input voltage 2 (Vw)	8500 V to 10000 V	
Output voltage (Vo)	9500 V to 10500 V	
Power rating	20 MW	
CUK converter	Inductor	LCUK = 1 $\mu$ H
	Capacitor	CCUK = 200 $\mu$ F
SEPIC converter	Inductor	LSEPIC = 2 mH
	Capacitor	CSEPIC = 10 mF
Integrated section	Inductor	Lo = 100 mH
	Capacitor	Co = 100 mF
Switching frequency	100 kHz	

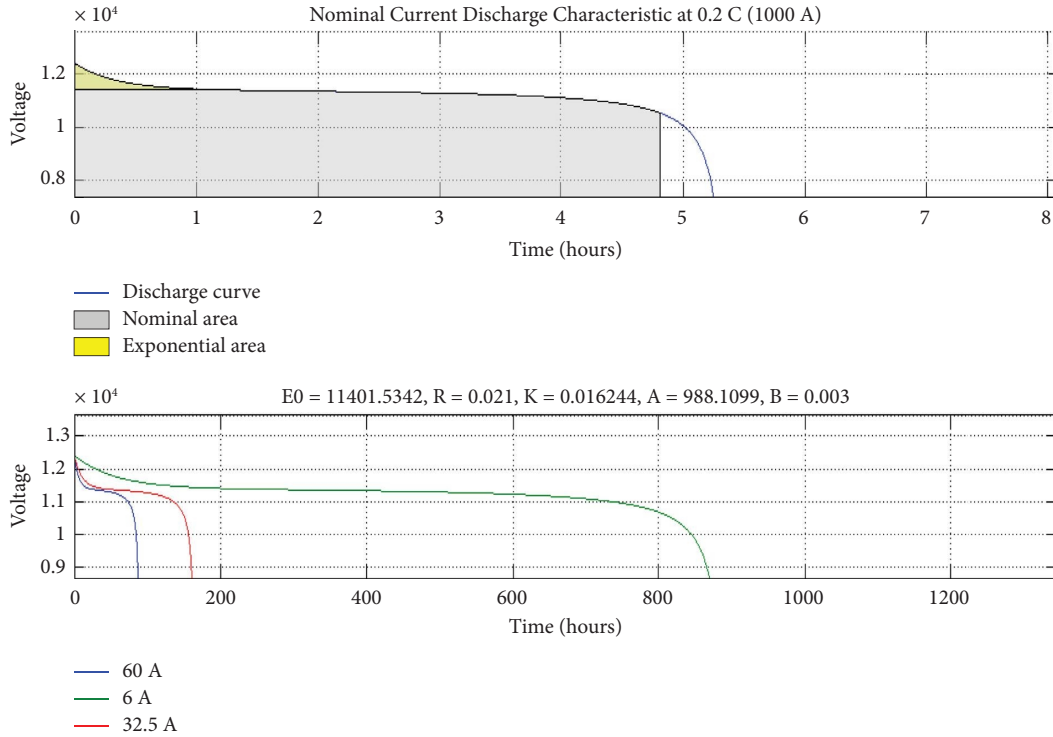


FIGURE 20: Discharging characteristics of the nickel-metal-hydride battery.

#### 4.1.1. Alternate Arm Converter Design

- Pr = 20 MW
- DC voltage  $V_{dc} = 10,000$  V
- Converter AC voltage  $V_{ac} = 10$  kV
- Arm inductor  $L_u$  and  $L_l = 100$   $\mu$ H
- Cell capacitance  $C_{SM} = 4$  mF
- Cell voltage  $V_{SM} = 1.5$  kV
- No. of submodules in arm  $N_{SM} = 9$
- No. of series director switch  $N_{dir} = 5$

A three-phase AAC is designed using MATLAB/Simulink. The full bridge submodules are designed with 4 IGBTs and a capacitor  $C_{SM}$  across each module. The IGBTs

in the submodules and in the director switches (DS) are triggered by the pulses generated using phase shift PWM technique with a switching frequency of 10 kHz. The pulses are generated using control strategies adopted which was already discussed in the methodology section. So, the pulses are provided to the IGBTs in the upper and lower arm by proper switching sequence of each phase which are switched on and off generating the three-phase AC output voltage with  $120^\circ$  displaced from each other. The DC voltage inputs to the AAC are supplied either from solar or wind or from the battery.

The grid is connected to the point of common coupling (PCC) to meet the load demand if in case the input from other sources is insufficient. The AC grid and the output of AAC are connected to PCC. Depending on the duty cycles

iso1 and iso\_grid generated by the energy management controller, either the grid or AAC feeds the loads. The grid will satisfy the load requirements or charge the battery depending on the duty cycle (iso1). A resistive load of rating 850 kW and an inductive load of  $R = 100$  kW and  $Q_r = 1000$  VAR are connected to PCC. Thus, the load demand is satisfied by the implementation of the energy management controller in the integration of microgrid, AAC, and AC grid.

**4.2. Energy Management System Controller.** The energy management system controller operates in 5 modes which generate the necessary control/duty cycle to operate the integrated CUK-SEPIC converter, either charge or discharge the battery, and feed the load either from a microgrid or an AC grid as shown in Table 3.

The controller is initialized and it receives the output voltages and currents of the solar PV system ( $V_s$ ,  $I_s$ ), wind ( $V_w$ ,  $I_w$ ), battery ( $V_b$ ,  $I_b$ , and SoC), and load ( $I_l$  and  $V_o$ ) to generate the duty cycles ( $ds1$ ,  $dw1$ ,  $db1$ ,  $db01$ ,  $iso1$ , and  $iso\_grid$ ) to operate the CUK-SEPIC converter and battery. The controller and entire proposed design are analysed for a time period of 0 to 2 seconds. Initially, both solar and wind energies are sufficient to feed the load which appears across the fused CUK-SEPIC converter for a time duration of 0 to 0.4 seconds. The duty cycles  $ds$ ,  $dw$ ,  $iso\_grid$ , and  $db01$  triggers the switches in the integrated CUK-SEPIC converter and supply a regulated input voltage of 10 kV across AAC. The battery is charged from 0 to 1.2 seconds by the ac grid which is controlled by the duty cycle  $db0$ . The output voltage from AAC feeds the load demand which is being controlled by the duty cycle  $iso\_grid$  which isolates the load from the grid for a duration of 0 to 1.6 seconds.

From 0.4 to 0.8 seconds, only solar output is available, and only the CUK converter generates 10 kV across AAC. During 0.8 to 1.2 seconds, only wind output is available, so only the SEPIC converter generates the 10 kV at the common point of the integrated CUK-SEPIC converter which is given as input to AAC. The battery alone discharges the stored energy to AAC during 1.2 to 1.6 seconds when the switch connected across the battery is triggered by the duty cycle  $db$ . The microgrid and AAC are isolated from the grid for a duration of 1.6 to 2 seconds which is controlled by the duty cycle  $iso$  given to the circuit breakers. The grid alone feeds both the loads and stops charging the battery during this period. Thus, the energy management controller regulates and manages the power flow through the entire system without any interruption in meeting the load demand.

## 5. Results and Discussion

The proposed AAC's suggested BFOA-trained FOPID controller has also been modelled and analysed using a MATLAB/Simulink model, and the results of the examination are reported. The simulation parameters of the solar, wind, AAC converter, filter, and battery circuit are listed in Table 4. A solar module for  $1 \text{ kW/m}^2$ , 54.7 V, a current rating

TABLE 3: Modes of operation of energy management controller.

Mode	Availability of energy sources feeding load	Simulation time duration
1	Both solar and wind connected	0–0.4 seconds
2	Solar	0.4–0.8 seconds
3	Wind	0.8–1.2 seconds
4	Battery	1.2–1.6 seconds
5	Grid	1.6–2 seconds

of 5.58 A, and the power of each module are chosen as 305 W. A wind speed of 12 m/s is chosen as the wind velocity. Two loads with capacities of 850 kW and 100 kW and reactive power of 1000 VAR are taken for simulation studies.

The waveforms of solar irradiance, the value of delta ( $\delta$ ) of the maximum power point tracking, solar PV voltage, its current curve, its output power, and the output voltage of the solar PV system with reference voltage are represented in Figures 21 and 22, respectively. It can be noted from the waveforms of the solar voltage and current that the values obtained matches with that of the rated values chosen for the simulation purposes. The entire energy management system with integration of solar, wind, battery, AAC, AC grid, and load is analysed for a time duration from 0 second to 2 seconds.

The wind velocity that swipes the wind turbine for a time duration from 0 second to 0.8 seconds is maintained at 8 m/s, the wind velocity of 12 m/s is maintained from 0.8 seconds to 1.2 seconds, and from 1.2 seconds to 2 seconds a wind velocity of 10 m/s is maintained. Based on the wind velocity, the outputs of the wind energy conversion system (WECS) are analysed. The performance parameters like the output voltage and output current of the wind farm, the AC-DC converter, the WECS-rated wind speed, and the variation of the output power are displayed in Figure 23. The output voltage of the AC-DC converter represents the rated value of 10 kV, and it is noted that the voltage contains less ripples. From Figure 23, it can be detected that the WECS output power reaches a peak of 50 MW before it settles nearly around 25–30 MW during the time period between 0 second and 0.4 seconds. The duty cycle  $dw1$  generated by the energy management controller is maintained at zero for analysis purpose so the power generated from WECS during time period from 0.4 seconds to 0.8 seconds is zero. During the time period between 0.8 seconds and 1.2 seconds, approximately 40 MW of power is generated by the WECS. The output power is again zero during 1.2 seconds to 2 seconds as the duty cycle  $dw1$  is again maintained at zero.

The fuzzy logic controller generates a pulse based on the duty cycles  $ds1$  and  $dw1$  to trigger the MOSFET/IGBT switches M1 and M2. An output voltage of 9 kV–10 kV appears across the point of common coupling of the integrated CUK-SEPIC DC-DC Converter. The output voltage is maintained around 9 kV–10 kV by the combined output voltage of solar and wind for the duration from 1 second to 0.4 seconds, and solar only contributes between 0.4 seconds and 0.8 seconds. During the time period 0.8 seconds–1.2 seconds, the output power is contributed only by the wind system which is presented in Figure 24.

TABLE 4: Design parameters of the proposed configuration.

Parameters	Values
Number of solar cells per module	96
Number of series-connected solar modules per string	183
Number of parallel strings of solar modules	1500
Wind speed	12 m/s
Wind power	70 MW
Wind generator voltage	10,000 V
DC voltage (Vdc)	10,000 V
Converter AC voltage (Vac)	10 kV
Arm inductor (Lu and Ll)	100 $\mu$ H
Cell capacitance (Ccell)	4 mF
Cell voltage (Vcell)	1.5 kV
No. of cell in arm (Ncell)	9
No. of series director switch (Ndir)	5
Snubber capacitance (Csn)	0.5 $\mu$ F
Snubber resistance (Rsn)	5 k $\Omega$
Switching frequency (fs)	15 kHz
Battery voltage	10.5 kV
Batter rating	5000 Ah

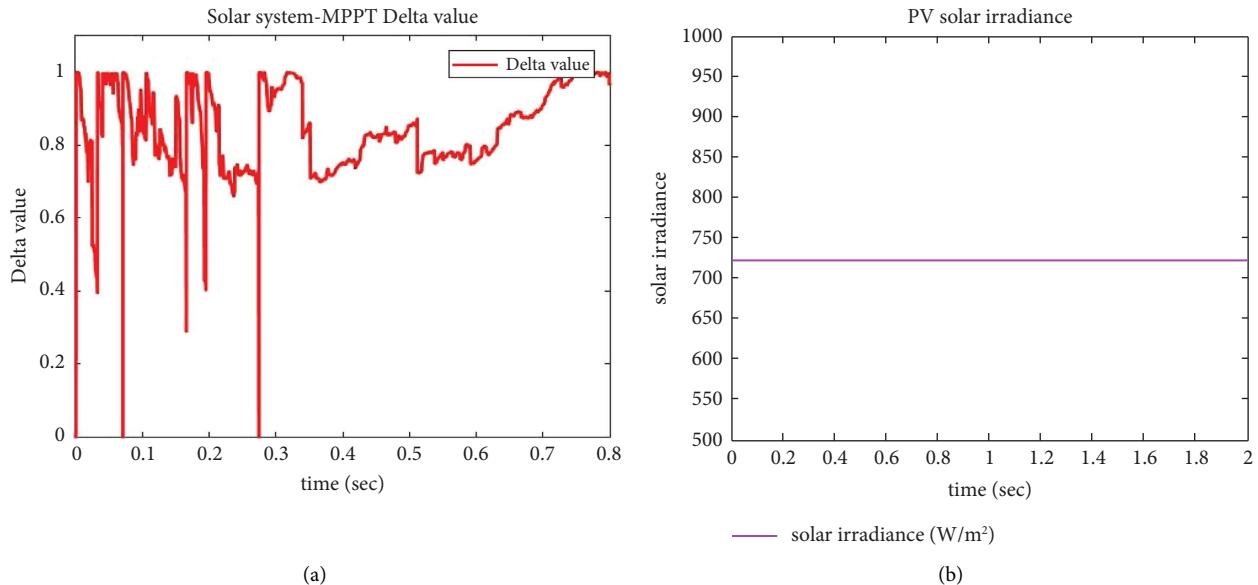


FIGURE 21: (a) Delta value for MPPT of the solar PV system and (b) solar irradiance.

Figure 25 depicts the battery voltage and current and the state of charge (SoC) of the battery. Initially, from 0 second to 1.2 seconds, the battery is charged by the AC grid which is initiated by the duty cycle db01. Based on the duty cycle db1, the battery delivers an output voltage of 10 kV to AAC for a time period between 1.2 seconds and 1.6 seconds, so that the SoC reduces from 50% to around 49.955%.

Figure 26 shows the waveforms of the energy management system. The energy management controller generates duty cycles (control signals) to initiate and trigger the switches to operate such that initially input voltage to AAC is provided by both solar and wind systems for a time period of 0.4 seconds at the common point terminals across the CUK-SEPIC converter, then from 0.4 seconds to 0.8 seconds, only solar contributes output voltage to the common point

terminals. At 0.8 seconds to 1.2 seconds, the output voltage at the common point of the CUK-SEPIC converter is generated only by wind, and the remaining duration is from 1.2 seconds to 1.6 seconds and from 1.6 seconds to 2 seconds, the power is contributed by the battery system and from the AC grid. So, the load requirements are met by the output voltage of AAC with the inputs from renewable energy sources and the battery till 1.6 seconds and during which the grid is isolated from the load which is controlled by the duty cycles "iso\_grid" and "is01", but the grid charges the battery without being idle as commanded by the duty cycles "iso1" and "db01" produced by the energy management controller. The load demand is supplied by only the AC grid for the remaining period which is controlled by the duty cycle "iso1." The output of AAC and the AC grid are connected at

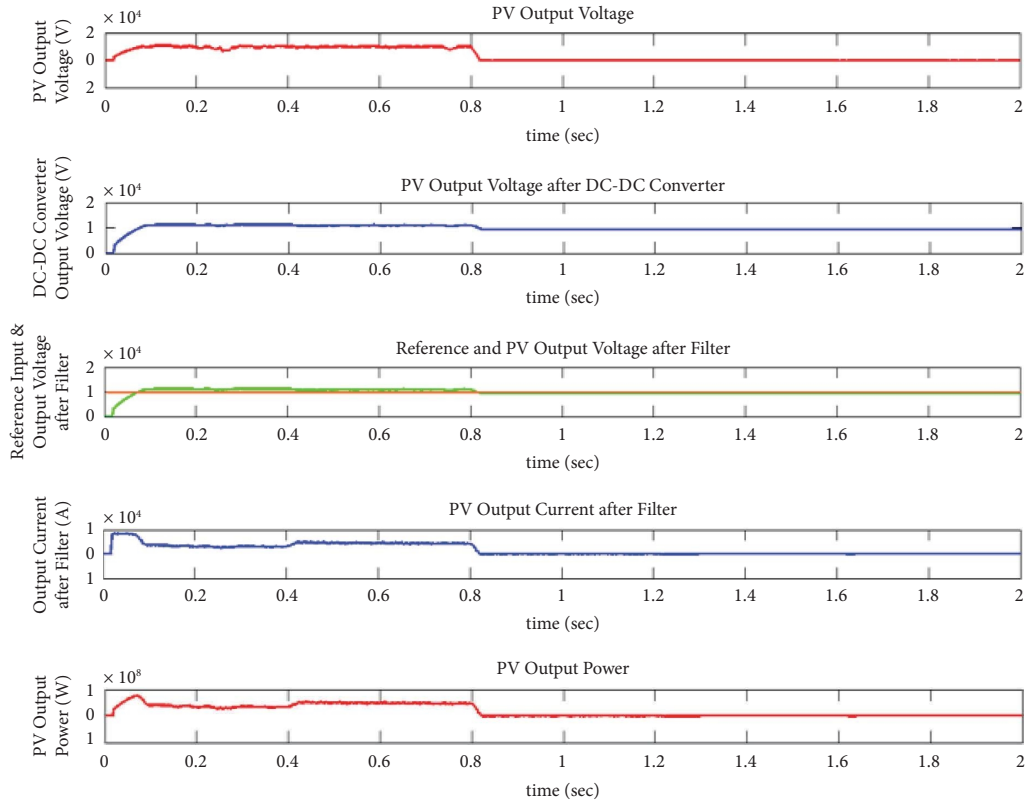


FIGURE 22: Solar PV system output voltage, current, and power.

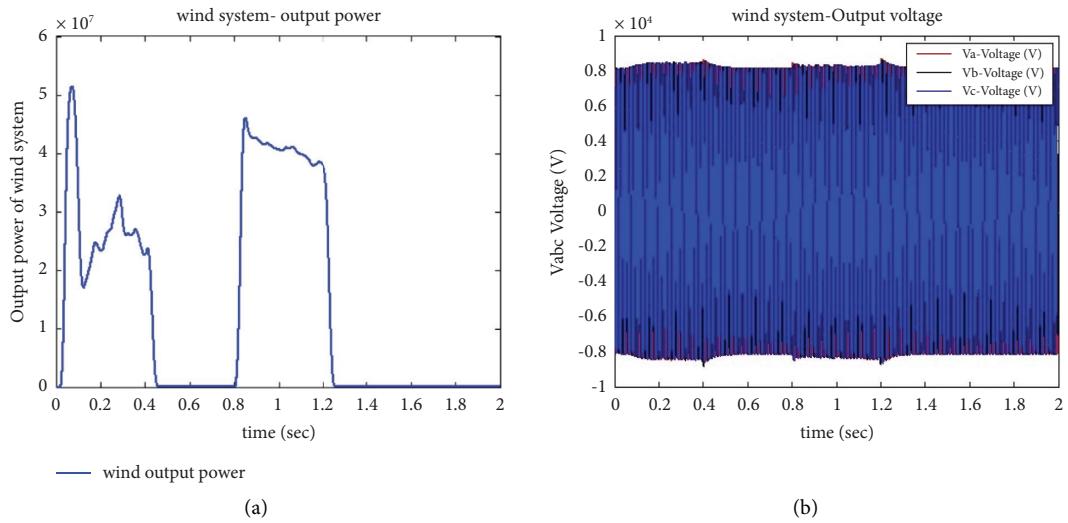


FIGURE 23: Continued.

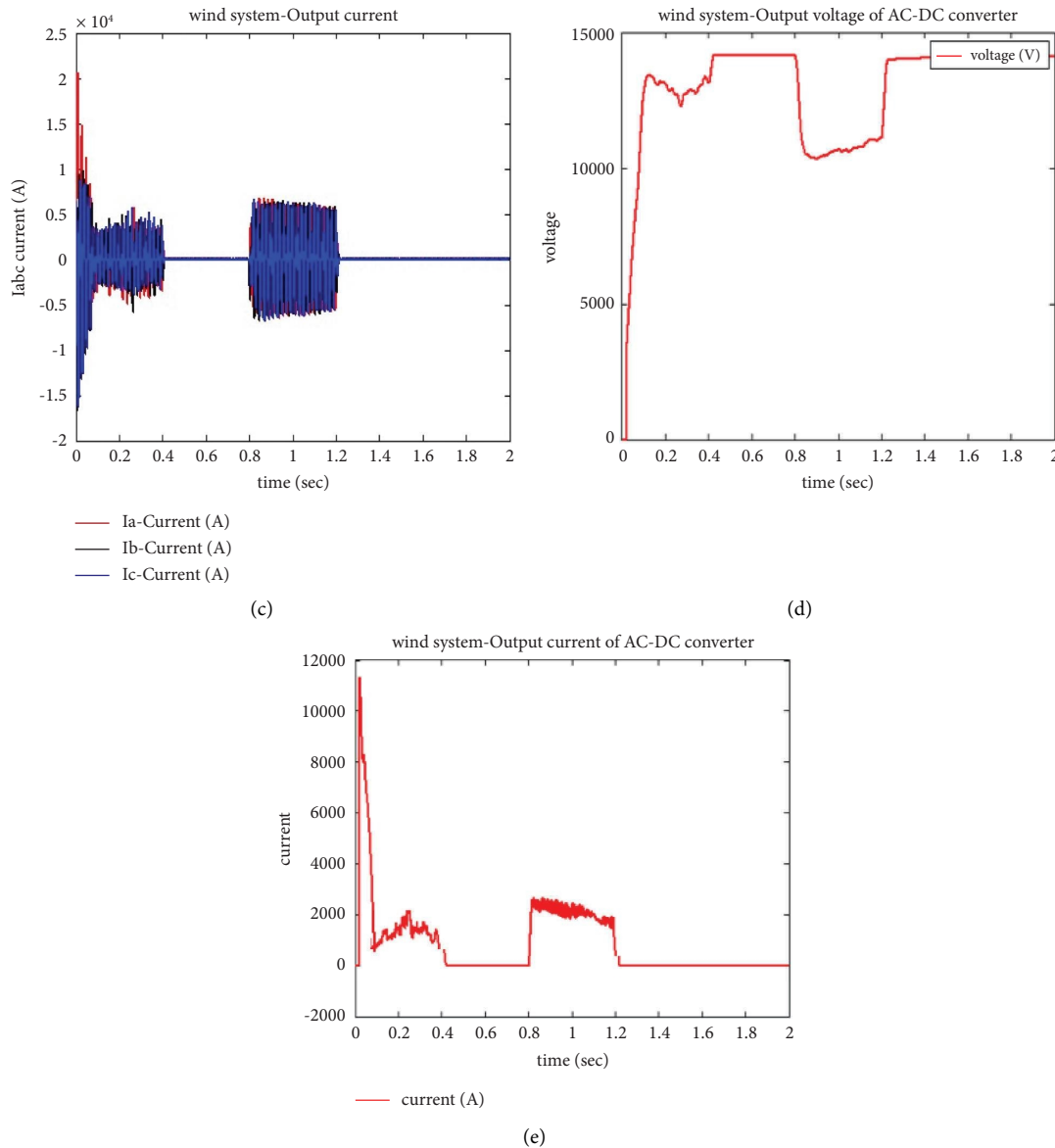


FIGURE 23: (a) Output power of WECS, (b) output voltage and (c) current, and (d) output voltage and (e) current of AC-DC converter.

the point of common coupling (PCC2) and the load demand is satisfied by these energy sources which are optimized by the efficient energy management controller. Figure 27 shows the PWM pulses that are generated using the BFOA-FOPID method and are applied to the DS of the AAC, and the corresponding circulating currents that are generated in the 3 legs of the AAC are depicted in Figure 28.

The circulating currents arise due to an unbalance in the submodule capacitor voltages which must be reduced and it constitutes a greater portion in increase of the power loss in the converter. Around 100 A of circulating current is flowing in each phase. The average capacitor potential for upper and lower submodules of the AAC is presented in Figure 29. The upper and lower arm current, internal circulating current of "a", "b", and "c" phases, and the voltage across the director switch of upper arm of "a" phase are shown in Figure 30.

The output voltage and current of a three-phase AAC configuration are illustrated in Figure 31. The voltage obtained at the output terminal of AAC is fed to meet the load demand. Two industrial loads, Load 1 and Load 2, are connected to the PCC. The load demand is met either by renewable energy sources or battery or the AC grid which is controlled, regulated, and managed by the energy management system/controller. The waveforms of the output voltage, current, and power of AAC and power delivered by AAC and grid to Load 1 are displayed in Figure 32.

The waveforms of grid voltage and current are depicted in Figure 33, and the output voltage, current, and the power of load 2 and power delivered by the grid are represented in Figure 34. It can be witnessed from the graphs of the current and voltage waveforms that all the graphs are nearly sinusoidal in quality; henceforth, it can be presumed that the THD of the proposed system is very less. The simulation



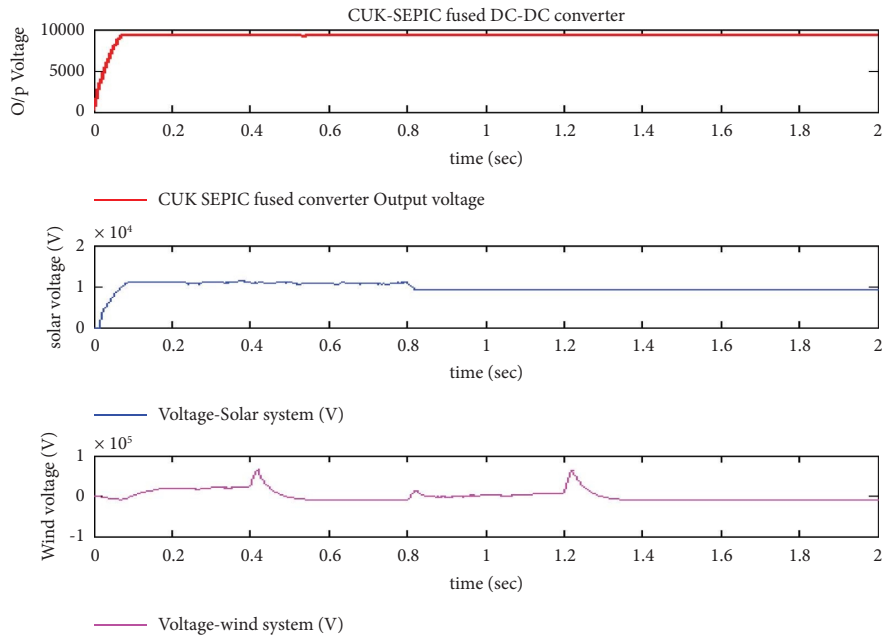


FIGURE 24: Output voltage of integrated CUK-SEPIC converter (fused DC-DC converter) at PCC1 and output voltage of solar and wind systems.

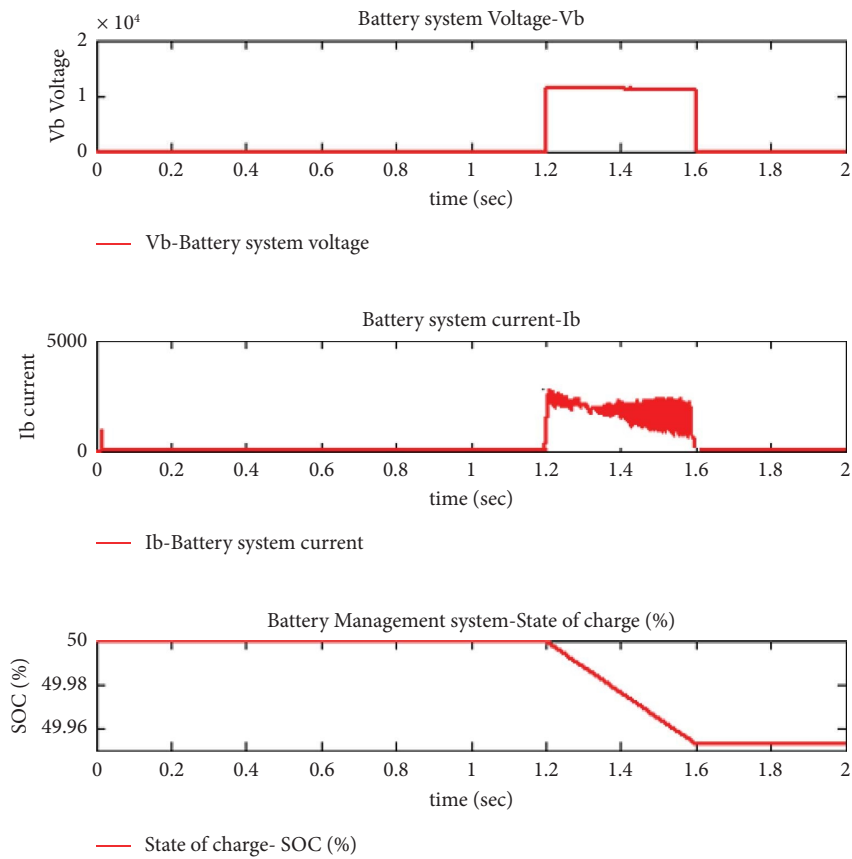


FIGURE 25: Battery system voltage, current, and SoC.

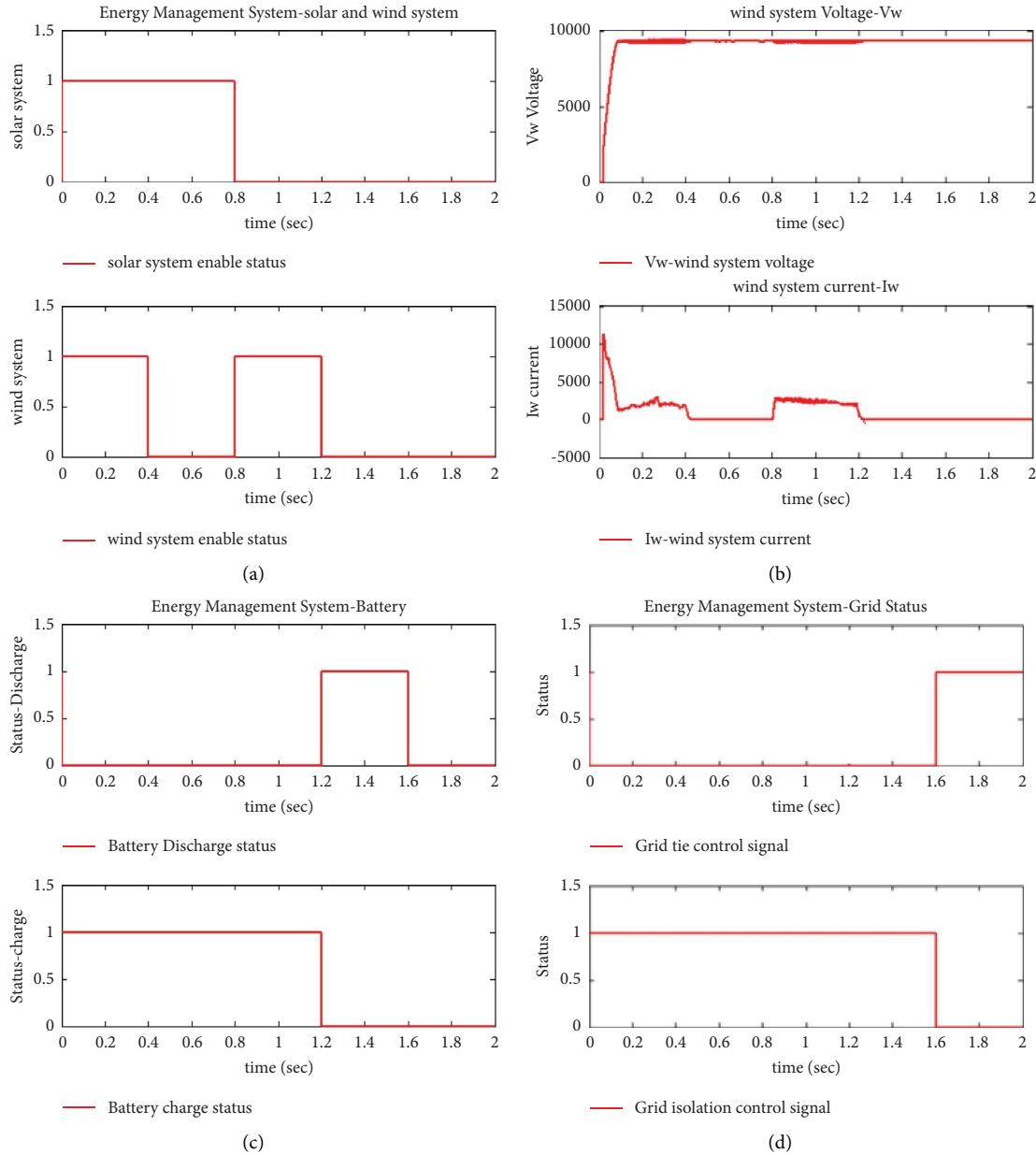


FIGURE 26: Energy management system waveforms.

consequences presented in Table 1 show that the error produced with the proposed BFOA methodology in tuning the FOPID is very less as compared to that of only the FOPID controller without the application of BFOA and PID controller in achieving the desired output voltage of 10 kV across AAC to meet the load demand without any interruption with the integration of various input sources controlled by an efficient energy management system.

Table 5 provides a comprehensive overview of the performance analysis conducted on a microgrid energy management system (EMS) across various time intervals. The microgrid refers to a comprehensive energy system that

integrates various energy sources and loads in order to guarantee a power supply that is both efficient and dependable. The table highlights the significant importance of the energy management system (EMS) in upholding the stability of the microgrid, effectively managing the equilibrium between energy supply and demand, and guaranteeing sufficient power allocation to different loads. The comprehensive data provided in the table facilitates comprehension of the microgrid's performance across various scenarios, thereby playing a crucial role in the development and enhancement of energy management strategies for practical implementations.

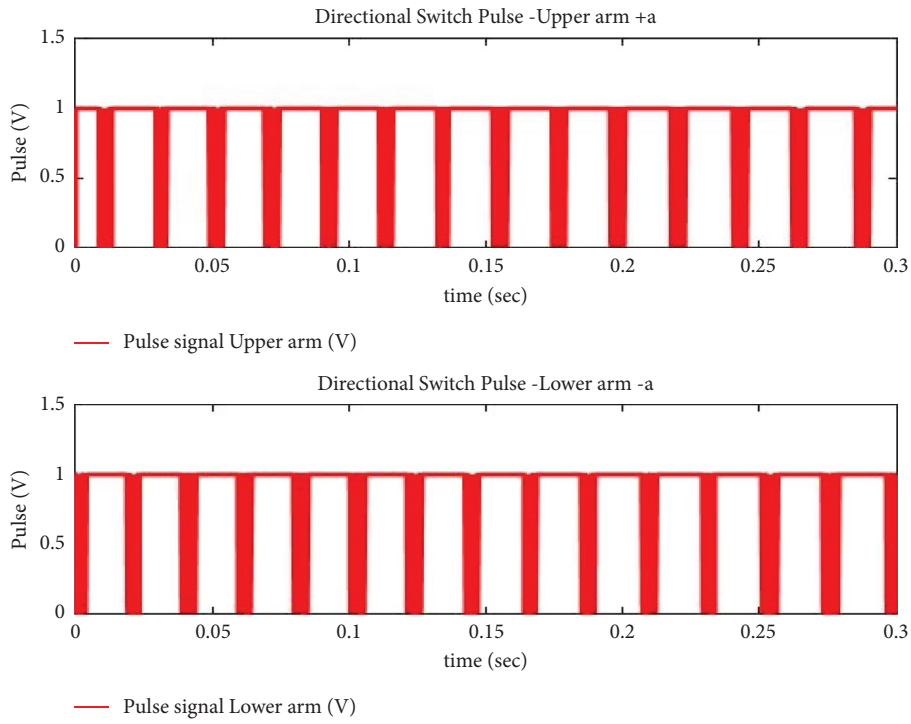


FIGURE 27: PWM pulses of DS of AAC.

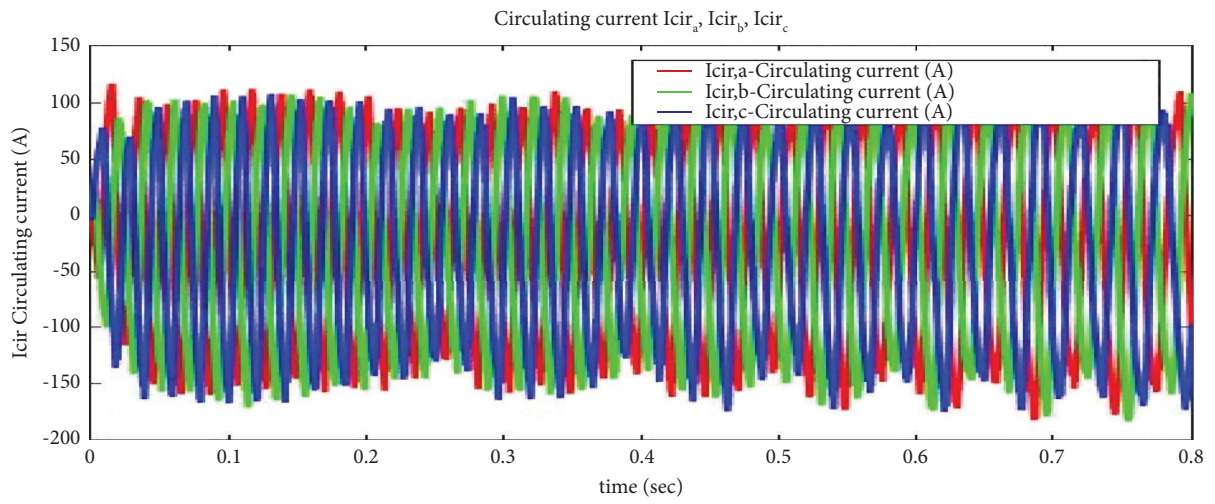


FIGURE 28: Circulating current of AAC.

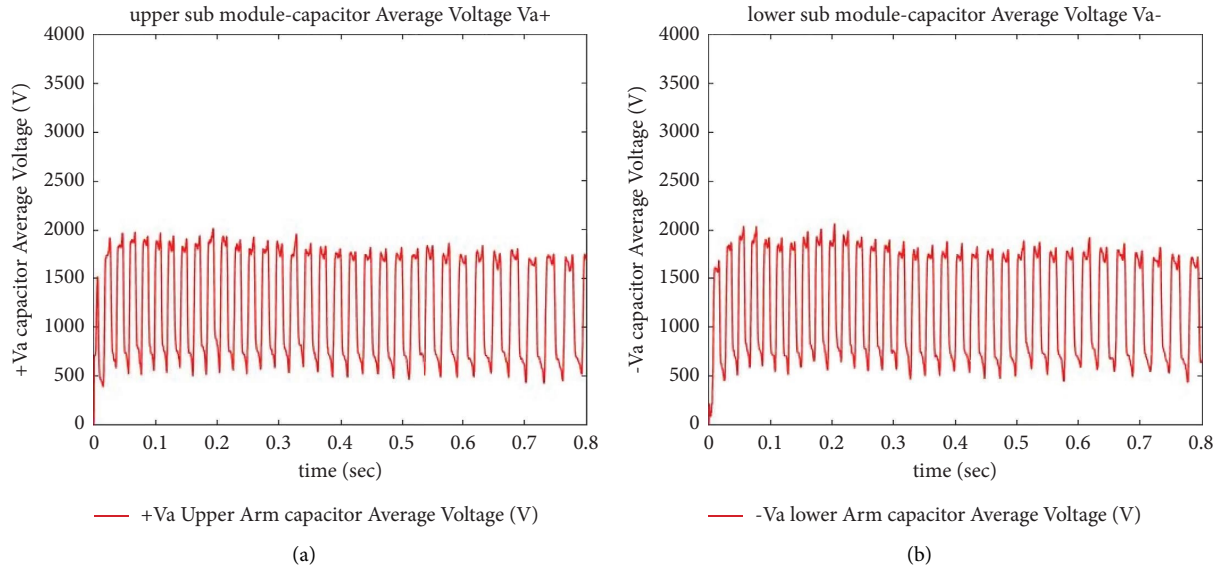


FIGURE 29: Average capacitor potential for 9 cells (upper SM and lower SM) of AAC.

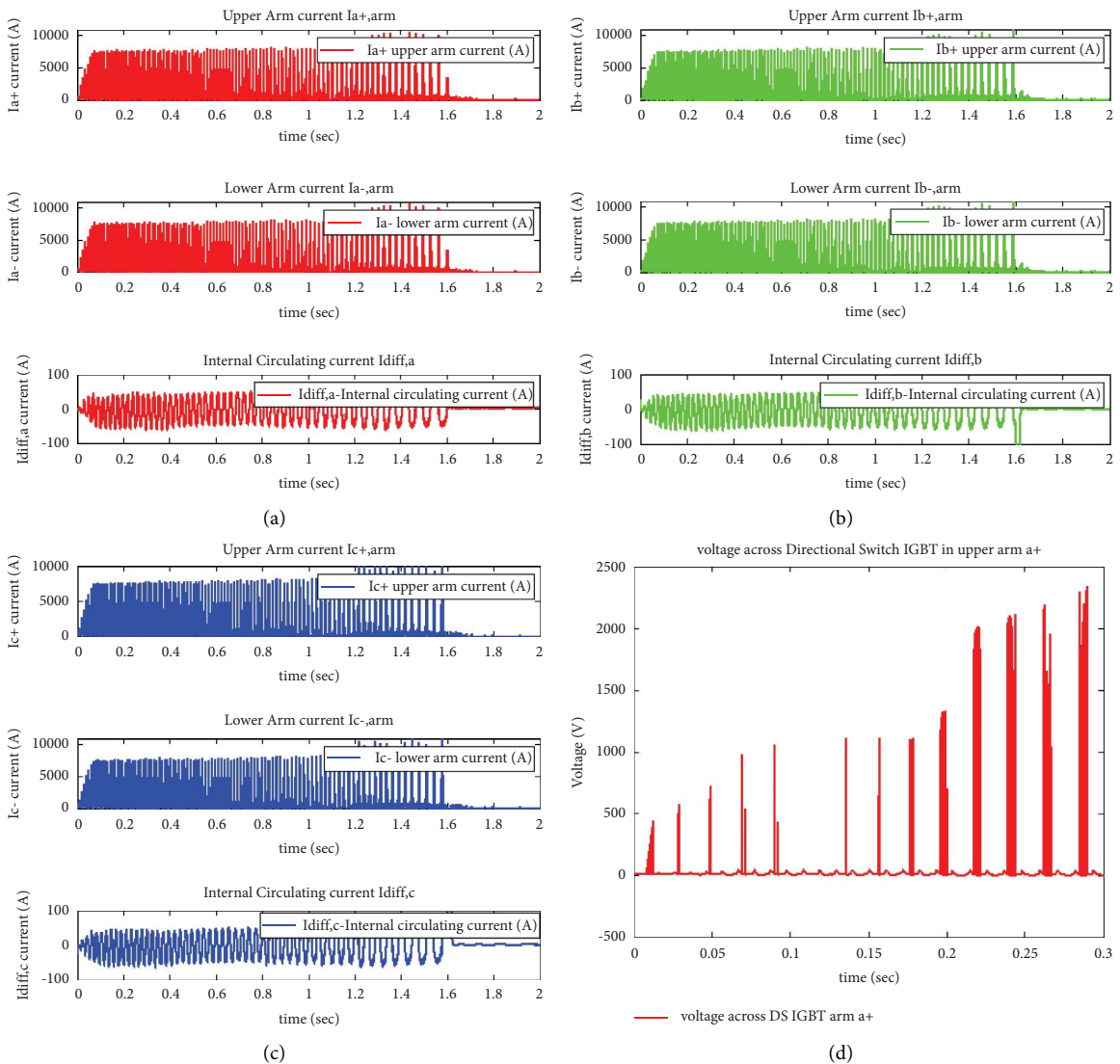
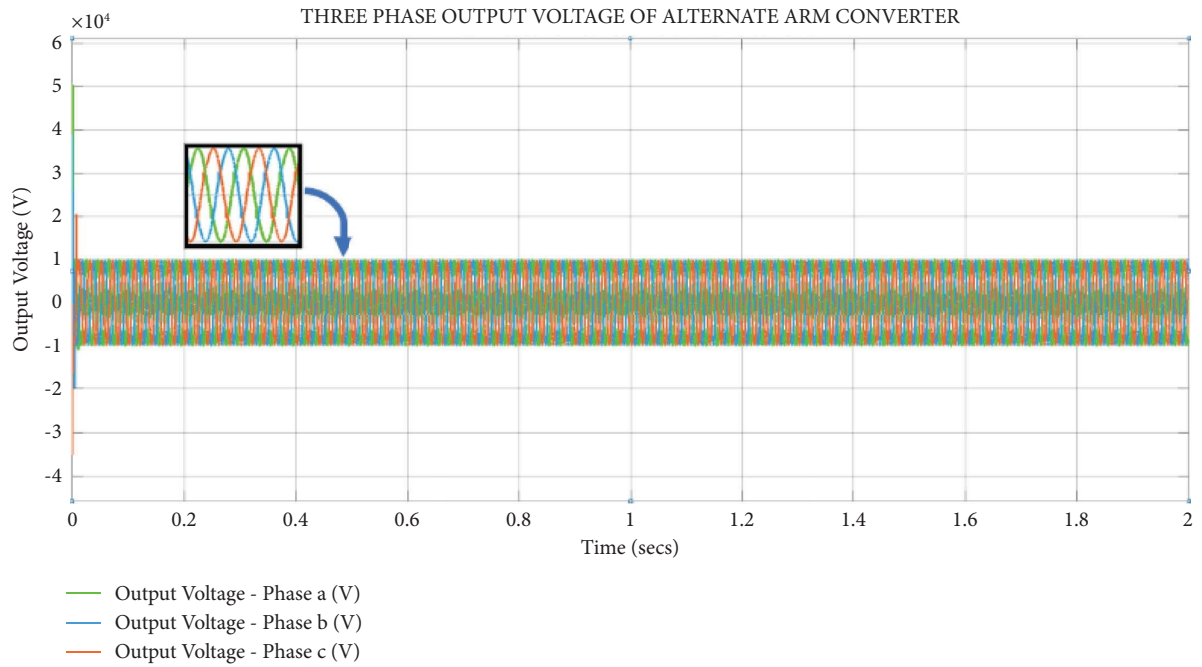
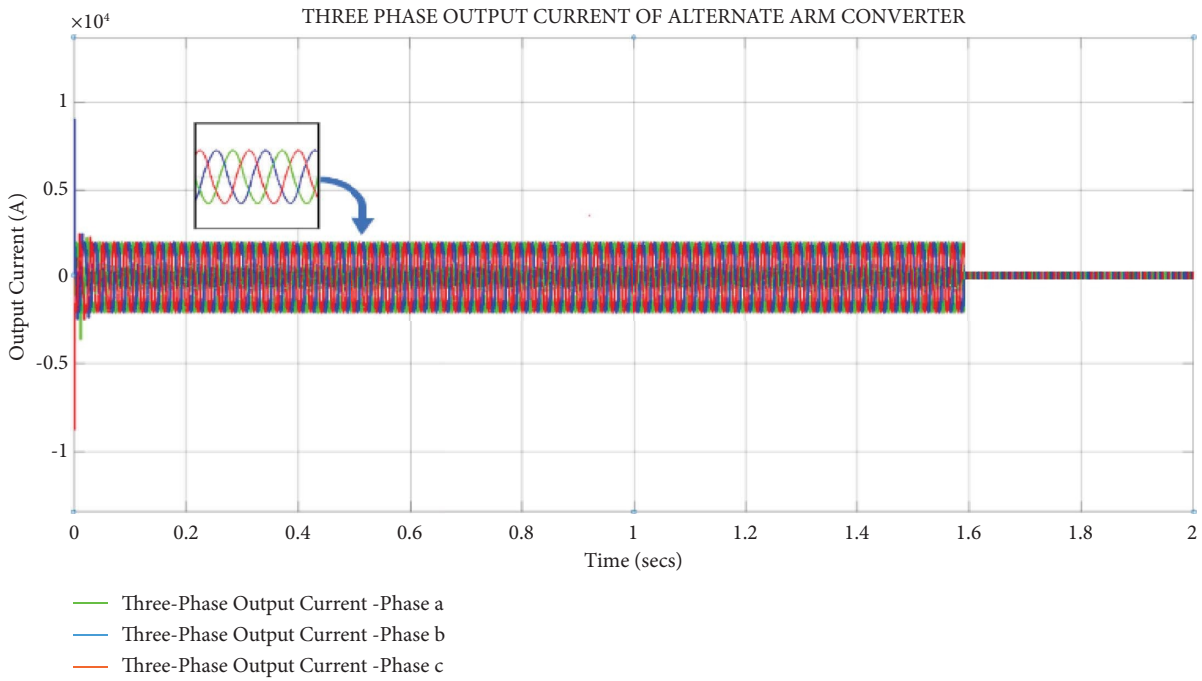


FIGURE 30: Upper and lower arm current, internal circulating current of A, B, and C phases, and voltage across director switch of phase A of upper arm in AAC.

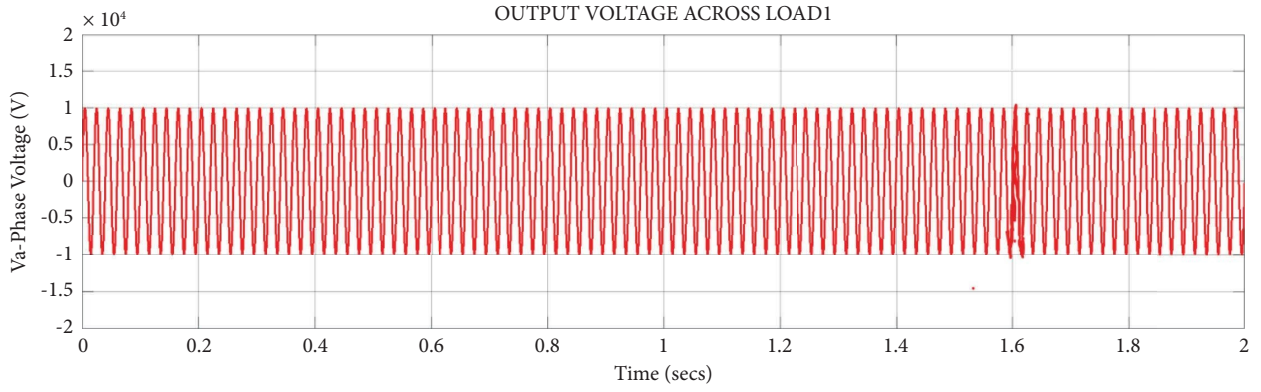


(a)



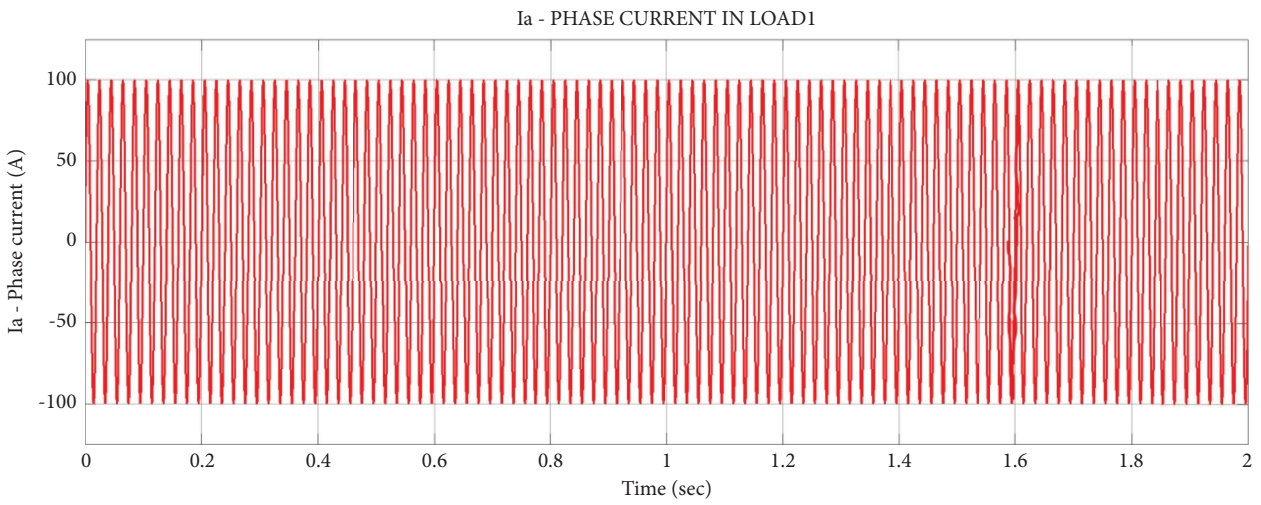
(b)

FIGURE 31: Three-phase output voltage and output current of AAC.



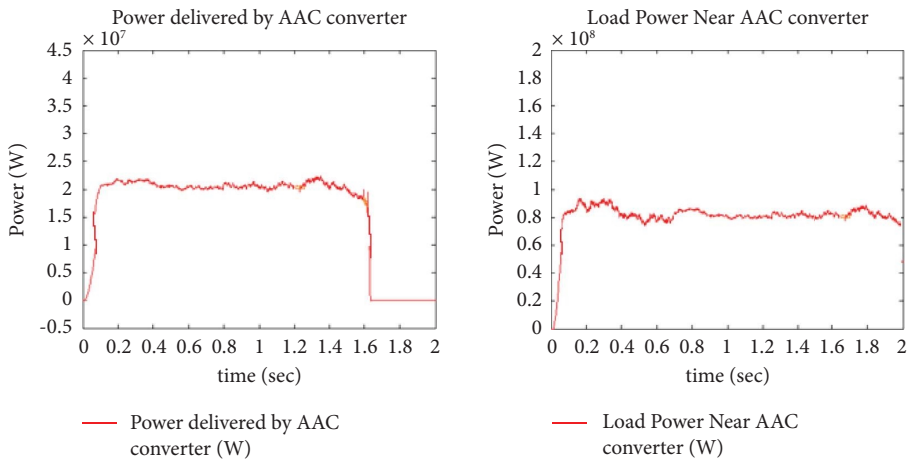
— Va- Phase Voltage

(a)



— Ia- Phase Current

(b)

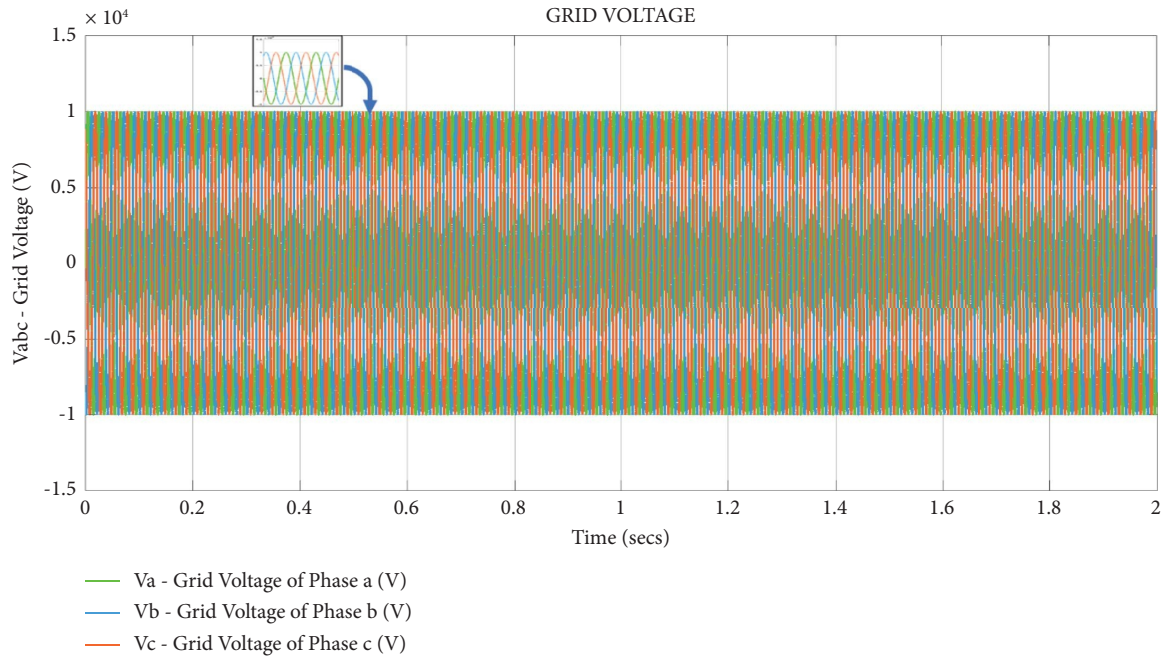


— Power delivered by AAC converter (W)

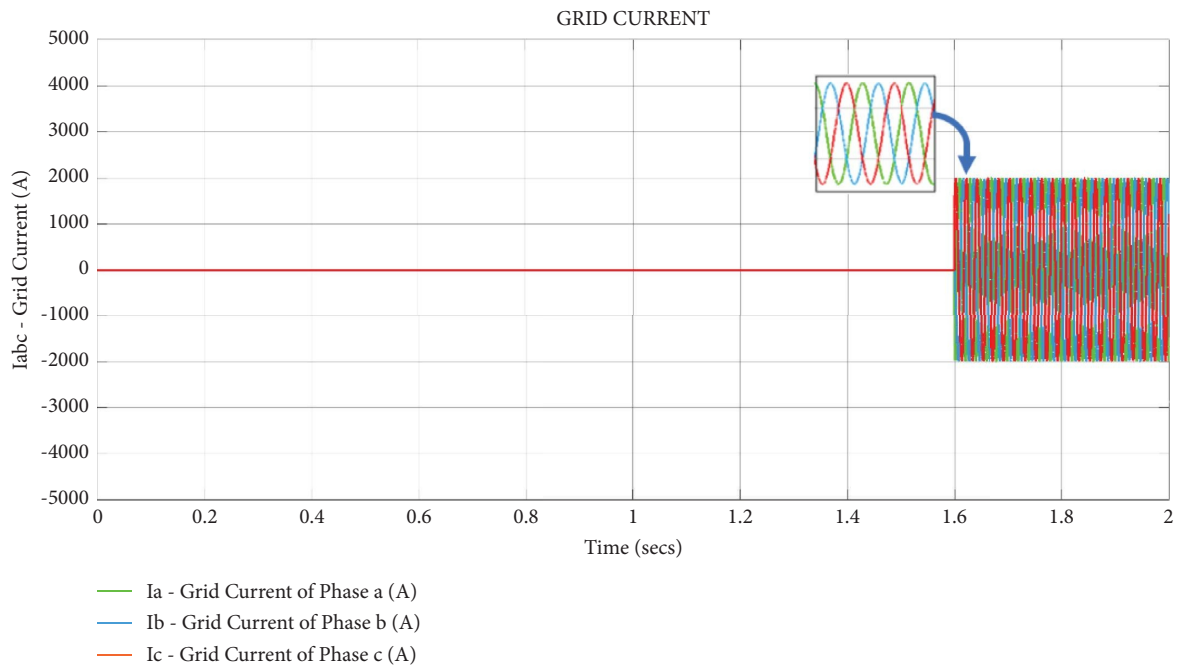
— Load Power Near AAC converter (W)

(c)

FIGURE 32: Output voltage, current, and the power of Load 1 and power delivered by AAC.

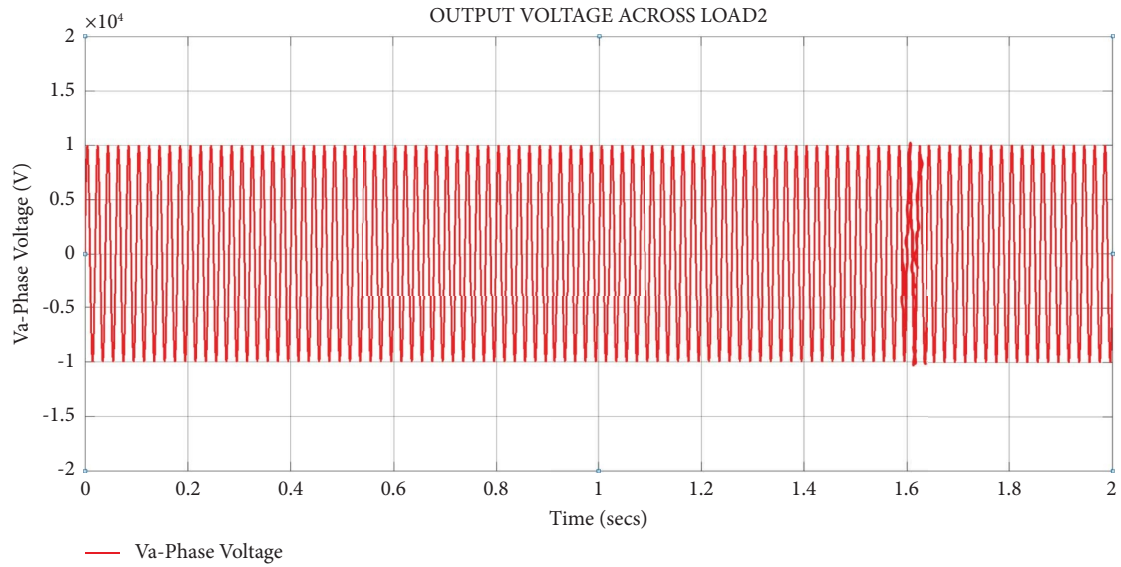


(a)

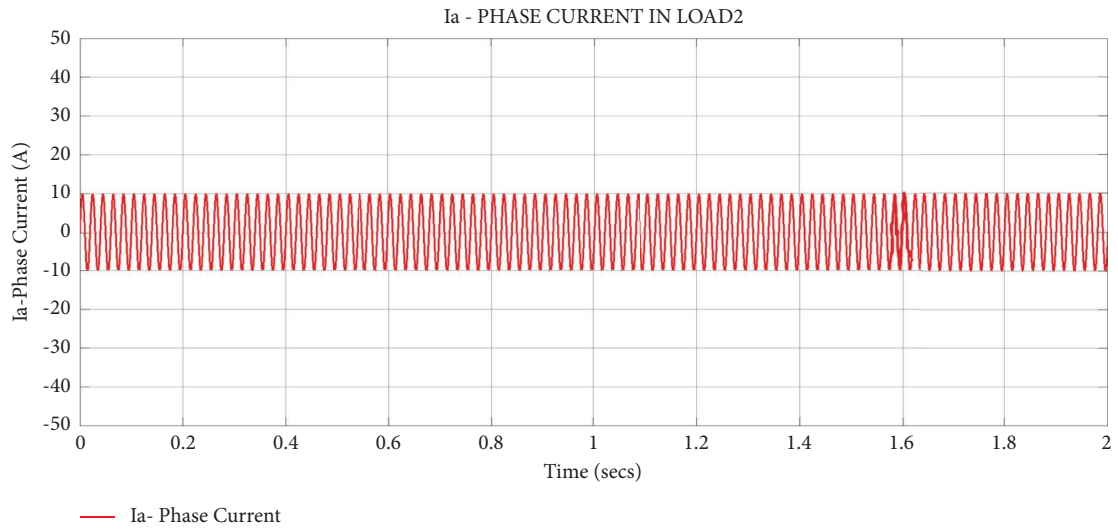


(b)

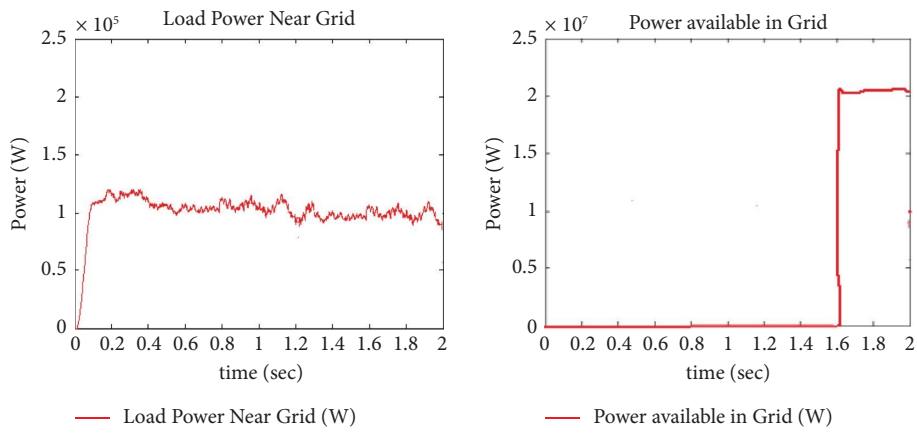
FIGURE 33: (a) Grid source voltage and (b) grid source current.



(a)



(b)



(c)

FIGURE 34: (a) Output phase voltage, (b) phase current, and (c) the power of Load 2 and power delivered by the grid.



TABLE 5: Performance analysis of microgrid using the energy management system.

Simulation time	Active sources	AAC input voltage (v)	AAC input current (A)	AAC input power (W)	AAC output voltage (V)	AAC output current (A)	AAC output power (W)	Load 1	Load 2
0-0.4 s	Solar + wind	11 kV	1650 A	18 MW				Power-850 kW	Apparent power-100 kVA
0.4 s-0.8 s	Solar	10.7 kV	1500 A	16 MW				Voltage-10 kV	Active power-100 kW
0.8 s-1.2 s	Wind	10.5 kV	1500 A	16 MW	10 kV	2000 A	20 MW		Voltage-10 kV
1.2 s-1.6 s	Battery	10 KV	2000 A	20 MW				Current- 85 A	Current-10 A
1.6 s-2 s	Grid	10 KV (to loads)	2000 A (to loads)	20 MW (to loads)					

## 6. Conclusion

This paper investigated the design of an efficient control strategy for AAC and a comparative analysis of controllers based on performance and spectral analysis was performed. Next, an optimal energy management system was proposed for a system integrating the microgrid and utility grid incorporating an AAC as an inverter to meet the load demand. The parameters for the proposed system are selected based on the load demand considering different input energy sources, monitored, and controlled by an efficient energy management system based on various operating conditions of inputs, and the performance of the system is verified through the results. An optimized control strategy is incorporated in AAC to obtain a desired output across it. A metaheuristic algorithm, bacterial foraging optimization algorithm, is implemented to train the FOPID controller to achieve the desired output to meet the load demand. The load demand is satisfied either by the microgrid through AAC or the AC grid which is foreseen by the energy management system. An efficient energy management system has been designed, and the results have been verified through simulation. The work of this paper can be incorporated in the telecom industry and railway traction.

## Data Availability

The data used to support the findings of this study are included within the article.

## Conflicts of Interest

The authors declare that they have no conflicts of interest.

## References

- [1] A. R. Battula, S. Vuddanti, and S. R. Salkuti, "Review of energy management system approaches in microgrids," *Energies*, vol. 14, no. 17, p. 5459, 2021.
- [2] C. Chen, S. Duan, T. Cai, B. Liu, and G. Hu, "Smart energy management system for optimal microgrid economic operation," *IET Renewable Power Generation*, vol. 5, no. 3, pp. 258–267, 2011.
- [3] V. A. Ani, "Development of an intelligent power management system for solar PV-Wind-Battery-Fuel-Cell integrated system," *Frontiers in Energy Research*, vol. 9, Article ID 613958, 2021.
- [4] A. Hasankhani and S. M. Hakimi, "Stochastic energy management of smart microgrid with intermittent renewable energy resources in electricity market," *Energy*, vol. 219, Article ID 119668, 2021.
- [5] J. Naik, P. K. Dash, and R. Bisoi, "Optimized droop controller-based energy management for stand-alone micro-grid using hybrid monarch butterfly and sine-cosine algorithm," *Sustainable Energy Technologies and Assessments*, vol. 46, Article ID 101310, 2021.
- [6] M. M. Merlin, T. C. Green, P. D. Mitcheson et al., "The alternate arm converter: a new hybrid multilevel converter with dc-fault blocking capability," *IEEE Transactions on Power Delivery*, vol. 29, no. 1, pp. 310–317, 2014.
- [7] Electrical Technology, "Electric vehicle test systems," <https://www.electricaltechnology.org>.
- [8] R. H. Chandio, H. M. Zawbaa, and S. Kamel, *Control and protection of MMC-Based HVDC Systems: A Review*, Elsevier, Amsterdam, The Netherlands, 2023.
- [9] N. Elisabeth, *Modelling and Control of the Modular Multilevel Converter*, Elsevier, Amsterdam, The Netherlands, 2012.
- [10] A. A. Mahmoud, A. A. Hafez, A. M. Yousef, M. A. Gaafar, M. Orabi, and A. F. M. Ali, "Fault-tolerant modular multilevel converter for a seamless transition between stand-alone and grid-connected microgrid," *IET Power Electronics*, vol. 16, no. 1, pp. 11–25, 2022.
- [11] C. Bajracharya, "Control of VSC-HVDC for wind power (Master's thesis)," Master's thesis, Norwegian University of Science and Technology, Trondheim, Norway, 2008.
- [12] E. Kabalci, *Multilevel Inverters: Control Methods and Advanced Power Electronic Applications*, Academic Press, Cambridge, MA, USA, 2021.
- [13] P. Sun, H. R. Wickramasinghe, and G. Konstantinou, "An LCC-AAC hybrid high-voltage DC transmission system," in *Proceedings of the 2020 IEEE 9th International Power Electronics and Motion Control Conference (IPEMC2020-ECCE Asia)*, pp. 1516–1521, IEEE, Nanjing, China, November 2020.
- [14] H. R. Wickramasinghe, P. Sun, and G. Konstantinou, "Interoperability of modular multilevel and alternate arm converters in hybrid HVDC systems," *Energies*, vol. 14, no. 5, p. 1363, 2021.
- [15] D. Dembinskas, "Modeling, simulation, and control of the alternate arm converter," Master's thesis, NTNU, Trondheim, Norway, 2017.
- [16] Digikey, "Synchronizing small-scale PV systems with the grid," 2015, <https://www.digikey.in/en/articles/synchronizing-small-scale-pv-systems-with-the-grid>.
- [17] M. J. Mohamed and A. Khashan, "Comparison between PID and FOPID controllers based on particle swarm optimization," in *Proceedings of the Second Engineering Conference of Control, Computers and Mechatronics Engineering*, Spain, July 2014.
- [18] W. Weisstein, "Fractional Calculus," From MathWorld--A Wolfram Web Resource. <https://mathworld.wolfram.com/FractionalCalculus.html>.
- [19] A. Tepljakov, B. B. Alagoz, C. Yeroglu, and E. Gonzalez, *FOPID Controllers and Their Industrial Applications: A Survey of Recent Results*, Elsevier, Amsterdam, The Netherlands, 2018.
- [20] C. Garcia, *Performance Comparison between IOPID and FOPID Controllers in an Industrial Flow Plant*, Elsevier, Amsterdam, The Netherlands, 2021.
- [21] S. M. AmlanBasu and R. Sharma, "Designing of the PID and FOPID controllers using conventional tuning techniques," in *Proceedings of the International Conference on Inventive Computation Technologies (ICICT)*, IEEE, Coimbatore, India, August 2016.
- [22] C. Guo, H. Tang, and B. Niu, "A survey of bacterial foraging optimization," *Neurocomputing*, vol. 452, pp. 728–746, 2021.
- [23] A. Mohamed Imran and M. Kowsalya, "Optimal size, and siting of multiple distributed generators in distribution system using bacterial foraging Optimization," *Swarm and Evolutionary Computation*, vol. 15, pp. 58–65, 2014.
- [24] B. Selva Rani and C. AswaniKumar, "A comprehensive review on bacteria foraging optimization technique," *Studies in Computational Intelligence*, vol. 592, 2015.
- [25] S. Balamurugan and S. Nageswari, "Circulating current control of modular multilevel converter by wild spider foraging optimization based fractional order proportional integral derivative controller," *Journal of Intelligent and Fuzzy Systems*, vol. 41, no. 2, pp. 4127–4147, 2021.

- [26] S. Govindugari Venkata, V. Ganesh, and S. Madichetty, "Application of bacteria foraging algorithm for modular multilevel converter-based microgrid with effect of wind power," *Electrical Engineering*, vol. 100, no. 3, pp. 2023–2036, 2018.
- [27] W. M. Amutha and V. Rajini, "Real-time energy management system for solar-wind-battery fed base transceiver station," in *Proceedings of the International Conference on Artificial Intelligence, Smart Grid and Smart City Applications*, pp. 109–121, Springer, Coimbatore, India, January 2020.
- [28] B. Mangu, K. Kumar, and B. G. Fernandes, "Efficiency improvement of solar-wind based dual-input converter for telecom power supply," in *Proceedings of the 11th International Conference on Environment and Electrical Engineering*, pp. 914–919, IEEE, Venice, Italy, May 2012.
- [29] S. K. TriptiSaha and D. Kumar Jha, "Fused converter topology for wind-solar hybrid systems," in *Proceedings of the 2013 IEEE PES Asia-Pacific Power and Energy Engineering Conference (APPEEC)*, Hong Kong, China, December 2013.
- [30] S. Shyni and R. Ramadevi, "A fused CUK-SEPIC converter topology for solar/wind hybrid standalone system," *Sathyabama Institute of Science and Technology, Chennai, Turkish Journal of Computer and Mathematics Education*, vol. 12, no. 7, pp. 2437–2448, 2021.
- [31] K. ZainulAbdin and R. Khalilpour, "Single and polystorage technologies for renewable-based hybrid energy systems," *Polygeneration with Polystorage for Chemical and Energy Hubs*, ScienceDirect, Amsterdam, Noord-Holland, The Netherlands, 2019.
- [32] J. M. German, "Hybrid electric vehicles," *Encyclopedia of Energy*, ScienceDirect, Amsterdam, Noord-Holland, The Netherlands, 2004.
- [33] Y. Y. Leow and C. A. Ooi, "Arm energy balancing control in AACs: a comparative analysis," *IET Power Electronics*, vol. 13, no. 6, pp. 1113–1128, 2020.
- [34] M. Zygmanski, B. Grzesik, and R. andNalepa, "Capacitance and inductance selection of the modular multilevel converter," in *Proceedings of the 2013 15th European conference on power electronics and applications (EPE)*, pp. 1–10, IEEE, Lille, France, September 2013.